Rachit Kumar

Automatic Radiometric Improvement of Moon Images for Shadow Segmentation

School of Electrical Engineering
Department of Electrical Engineering and Automation

Thesis submitted in partial fulfillment of the requirements for the degree of
Master of Science in Technology

Espoo, August 21, 2015

Instructor: Martin Lingenauber (Dipl.-Ing.)
German Aerospace Centre (DLR)
Department of Robotics and Mechatronics

Supervisors: Professor Arto Visala
Aalto University
School of Electrical Engineering

Professor Anita Enmark
Luleå University of Technology
Department of Computer Science

Preface

I want to thank Prof. Arto Visala for his support and guidance. I am grateful to German Aerospace Centre (DLR), Munich for the opportunity. I would like to extend my special gratitude to Martin Lingenauber and Hannah Kaufmann (German Aerospace Centre, DLR) for their guidance throughout my thesis. Their inputs were always inspiring and vital for the completion of this thesis.

I would also like to acknowledge the support of Maria Winneback (LTU) and Tomi Ylikorpi (Aalto University) throughout the space master program, I can not thank them enough. I am highly grateful to Rokon for taking care of the administrative work at university on by behalf.

Finally, I would like to thank the people who mean the world to me, my parents and my brother, their faith and love have been a constant source of energy for me.

Espoo, August 21, 2015

Rachit Kumar

Aalto University
School of Electrical Engineering Abstract of the Master's Thesis

Author:	Rachit Kumar
Title of the thesis:	Automatic Radiometric Improvement of Moon Images for Shadow Segmentation
Date:	August 21, 2015 **Number of pages:** 11 + 73
Department:	Department of Electrical Engineering and Automation
Programme:	Master's Degree Programme in Space Science and Technology
Professorship:	Automation Technology (AS-84)
Supervisors:	Professor Arto Visala (Aalto)
	Professor Anita Enmark (LTU)
Instructor:	Martin Lingenauber (DLR)

Kaufmann et al. [18] have proposed a method for pose estimation of the spacecraft during the descent phase by matching the shadows between real time images and pre-rendered reference images. The shadow segmentation of the real time images is largely affected by the Lunar surface reflectance, the Lunar surface topography, the Lunar surface features and the illumination conditions. This thesis investigates various radiometric enhancement methods to reduce the effect of these artefacts on the shadow segmentation. An enhancement pipeline was designed to enhance the contrast of the images. An automated classification of images was also implemented in the pipeline based on topographical information and mathematical parameters. Images taken with the Narrow Angle Camera (NAC) during the Lunar Reconnaissance Orbiter (LRO) mission were used to develop the automated classification logic of the pipeline and to validate the performance of the pipeline. The reference images were rendered based on the Digital Terrain Model (DTM) files of the corresponding NAC images.

The result shows that enhancement of the descent images increases the amount of segmented shadows, when compared with the shadow segmented original image. The percentage of correct shadow match between the shadow segmented virtual image and shadow segmented enhanced images are higher compared to the shadow segmented original image. Further, it is observed that the applied enhancement method depends on the surface reflectance and the incidence angle.

Keywords: image processing, optical navigation, shadow segmentation, radiometric enhancement, Lunar image classification

Contents

List of Figures

List of Tables

Symbols and abbreviations

Symbols

$\lfloor x \rfloor$	largest integer less than or equal to x
$f()$	input image
$g()$	enhanced image
$F()$	FT of input image
$G()$	FT of enhanced image
$B()$	Butterworth filter
o_x	offset in column
o_x	offset in row
mi	mile
m	meter
mm	millimetre
H	entropy
$p(x)$	probability of x
$p(x, y)$	normalised value at (x, y)
$c(x)$	cumulative probability of x
i	incidence angle
L	number of grey levels
i_f	image filter spatial domain
I_f	image filter frequency domain
V	GLCM matrix
$cont_v$	GLCM contrast
M_G	horizontal GLCM matrix
$P_v()$	normalised GLCM matrix
$corr_v$	GLCM correlation
h_v	GLCM entropy
M	number of rows of an image
N	number of columns of an image
$i()$	illumination component of image
$r()$	reflectance component of image
μ	mean
σ	standard deviation

Operators

$\sum_x$	sum over index x
$\mathcal{F}$	Fourier transform operator
$\mathcal{F}^{-1}$	inverse Fourier transform operator
$\leftarrow$	assign r-value to l-values

Acronyms

1 Introduction

The Lunar craters, regoliths and Lunar volcanic features (mare and terra) provide valuable information about the formation of the solar system. Future manned missions or settlement plans on Moon, makes it vital to have a better understanding of the surface of the Moon and find the presence of water. National Aeronautics and Space Administration (NASA) has enlisted several objectives [26] for future Moon exploration.

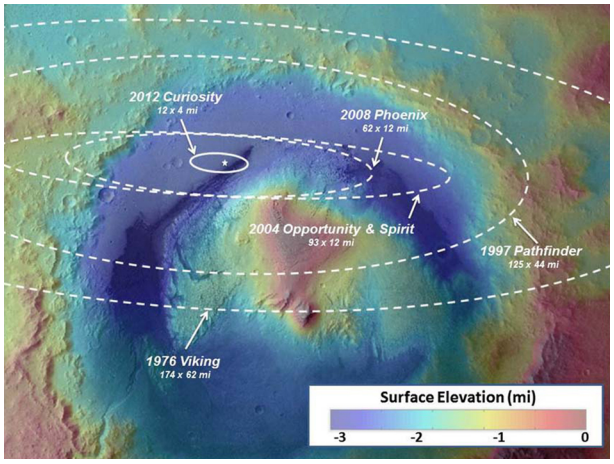

Figure 1.1: Landing accuracy of various Mars missions [28]

A historical perspective of the increase in landing accuracy of rover missions to Mars is provided by NASA [28] and shown in figure: 1.1. From an elliptical accuracy of 280×100 km in 1976 (Viking mission) to an accuracy of 19×6 km in 2012 (Curiosity mission), the precision has improved approximately 15 times. Although this seems like a big leap in landing accuracy, given the fact that remotely navigating a rover is risky and costs lot of time and money, a more cost efficient landing system (probably with accuracy in only hunderds of meters) would be efficient and save time for scientific experiments. Global Positioning System (GPS) is a promising option on Earth for position determination, but it is not available for the Moon. The most promising alternate option is to use terrain based optical navigation, and use landmarks for navigation guidance and control during the descent phase.

1.1 Background

Terrain based optical navigation augments the navigation capabilities of the state of art guidance and navigation control technology, by adding visual information. The visual information gathered from an on-board camera, exploits the geographical features of the landing site to enhance the landing precision of the robotic lander. The use of visual information also makes the system more autonomous and requires minimal assistance from the earth mission control centre. In addition, the visual system provides the capability to identify safe areas during the descent phase and

hence avoid a hazardous landing.

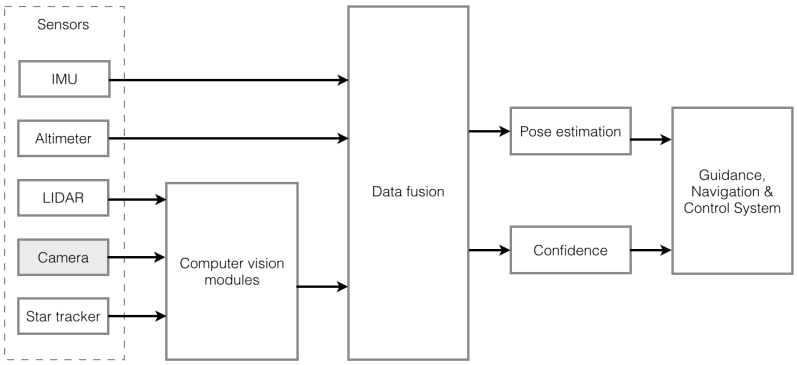

Figure 1.2: Basic representation of optical navigation system (based on Kaufmann [17])

Figure: 1.2 shows the basic representation of an optical navigation system. It combines data from an Inertial Measurement Unit (IMU), a Light Detection and Ranging (LIDAR), an Altimeter, a camera and a star tracker sensors by using computer vision modules and data fusion algorithms such as Kalman filter. The filter provides a pose estimate and a confidence measure to the Guidance Navigation and Control System (GNCS) system, which controls the landing trajectory of the spacecraft.

Autonomous navigation of a spacecraft based on visual information, has been proposed by various organisations. Autonomous Landing and Hazard Avoidance Technology (ALHAT) [13] proposed by NASA targets to have an accuracy of 90 m. Vision based navigation has also been proposed for aerial vehicles by Kaiser et al. [15] using Scale Invariant Feature Transform (SIFT) to detect and track features, from one frame to another locally and match identified features at global level. Optical Guidance for Autonomous Landing of Spacecraft (OGALS) [21] proposed by Japan Aerospace Exploration Agency (JAXA) to autonomously land on small celestial bodies, is based on surface features. The attitude of the spacecraft relative to the celestial body is computed using the range measurement and location of detected features on the descent image. The simulation results of the proposed method seemed to be accurate with a guidance error of 7.1 m, but the application of the method is limited to small bodies (like comets). Landing with Inertial and Optical Navigation (LION) proposed by European Space Agency (ESA) [6] uses 3D rendering of the surface and compares it with the built in digital elevation model to estimate the pose. The LION system also combines data from inertial sensors.

Autonomous Terrain based Optical Navigation (ATON) is an ongoing project at the German Aerospace Centre to develop a comprehensive closed loop system for localization and position estimation for future landing missions to the Moon. The ATON system fuses data from different on-board sensors together, using Kalman filter for a more robust, accurate and reliable pose estimation [17].

The ATON system combines the relative pose estimate of a feature tracker with the absolute pose estimates of a crater navigation module and a 3D matching pipeline. For

the last landing phase the Binary Shadow Matching (BSM) was recently proposed by Kaufmann et. al [18]. The BSM is based on the idea of using shadows as landmarks. As the Moon has virtually no atmosphere and as the surface of the Moon is covered with numerous shadow generating features such as craters and mountains. Due to these factors Moon has abundant and distinct shadows, which can be used as features. This supports the basic need of every matching and pose estimation, for as many features as possible to have a more robust and accurate solution.

As shown in figure: 1.3 a slight possible deviation from the planned trajectory is corrected based on the pose estimate computed by matching the shadows of a reference image with the shadows of an actual image taken during the descent phase. The pose estimate is fed to the GNCS and if required a course correction is performed to precisely land at the designated landing site.

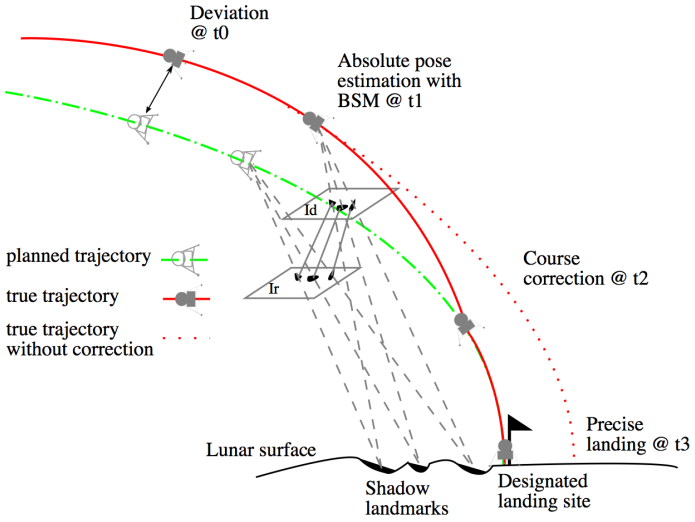

Figure 1.3: Application of binary shadow matching during descent phase (Kaufmann et al. [18])

Binary shadow matching

As shown in figure: 1.4, the BSM combines the shadow information from a rendered image and a descent image to estimate the pose of the spacecraft. A geo-referenced shadow map of the Lunar surface is created using the rendered images rendered from geo-referenced DTM files, based on the designated landing site and the planned landing trajectory. The BSM consists of four main processing steps: shadow segmentation, shadow description, shadow matching and pose estimation as illustrated by figure: 1.4. The shadows are segmented based on the maximum entropy thresholding proposed by Kapur et al. [16]. The result is a binary image referred as Binary Shadow Image (BSI), which only contains the shadow information of the images. Each shadow is described with its neighbouring shadows, by projecting their centroids to a two dimensional grid. Kaufmann et al. [18] have stressed the need of several grids with different resolution in a pyramidal structure as shown in figure: 1.4. The proposed pyramid structure has two advantages, it makes the system robust against different image resolutions and it speeds up the matching process. The matching

itself reduces to a simple binary comparison between the descriptor grids. Based on the matching result the pose is estimated.

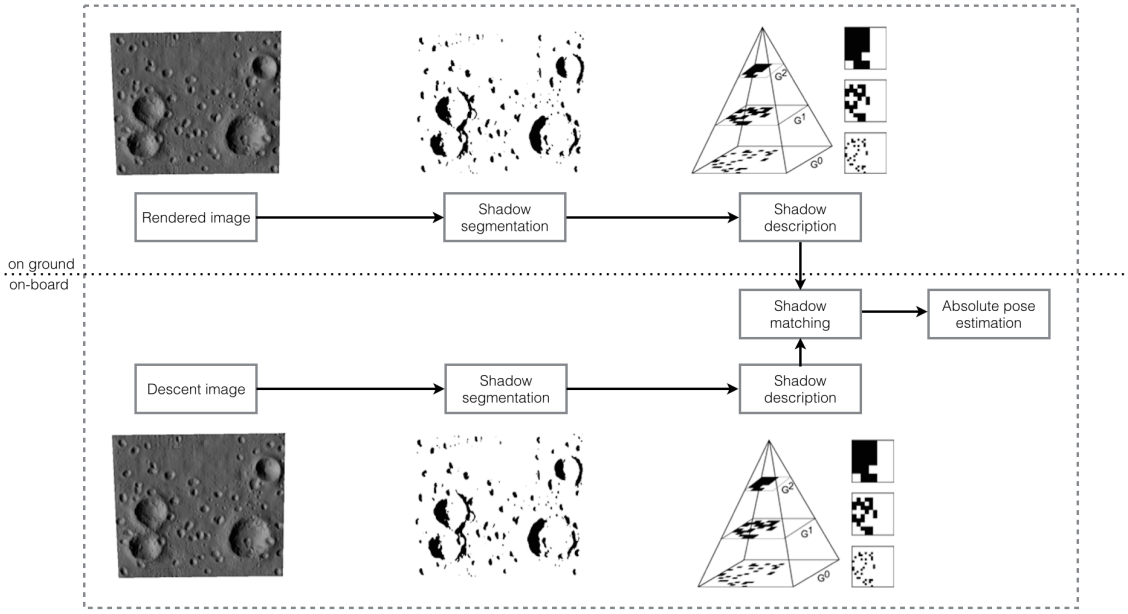

Figure 1.4: Binary shadow matching working principle (based on Kaufmann et al. [18])

1.2 Objective

The BSM was tested with virtually rendered images (from DTM) at different illumination conditions and trajectory shifts. To further test the robustness of the method, it was proposed to use recorded real mission data. Initial investigation suggested that the surface reflectance and surface features of Lunar surface vary from one region to another, which makes the shadow segmentation process very challenging. The performance of the BSM is directly related to the amount of detected shadow, hence it is imperative to detect the maximum number of existing shadows in a scene. To minimise the effect of aforementioned artefacts on the performance of BSM, it was decided to use a radiometric enhancement pipeline which would balance the information content of the image to improve the shadow segmentation.

Need for radiometric enhancement

The real time images of the Lunar surface can vary largely in surface reflectance and illumination condition during acquisition. New craters on the Lunar surface have high reflectance due to smooth surfaces, whereas old craters have relatively low reflectance. Mare regions of the Moon have a relatively dark surface which generates similar grey level values as shadow, and hence makes it difficult for an adaptive thresholding method to segment the shadows from the background. Figure: 1.5 shows an example of the same mare region using a rendered image, a real Lunar image and an enhanced Lunar image. The binary shadow image for each of the grey scale images is also shown. As shown in figure: 1.5, the total shadow count for the rendered

image is 33, and the total shadow count for the segmented image (original) is 5, where as the total shadow count for the enhanced image is 21. The shadow count considers only the shadows with a *contour area*[1] more than or equal to 10 *pixels*, as any shadow with a contour area less than 10 *pixels* is assumed to be insignificant to be considered as a feature. As this simple example shows, the number of shadows after enhancement of the image is much higher than for the original image.

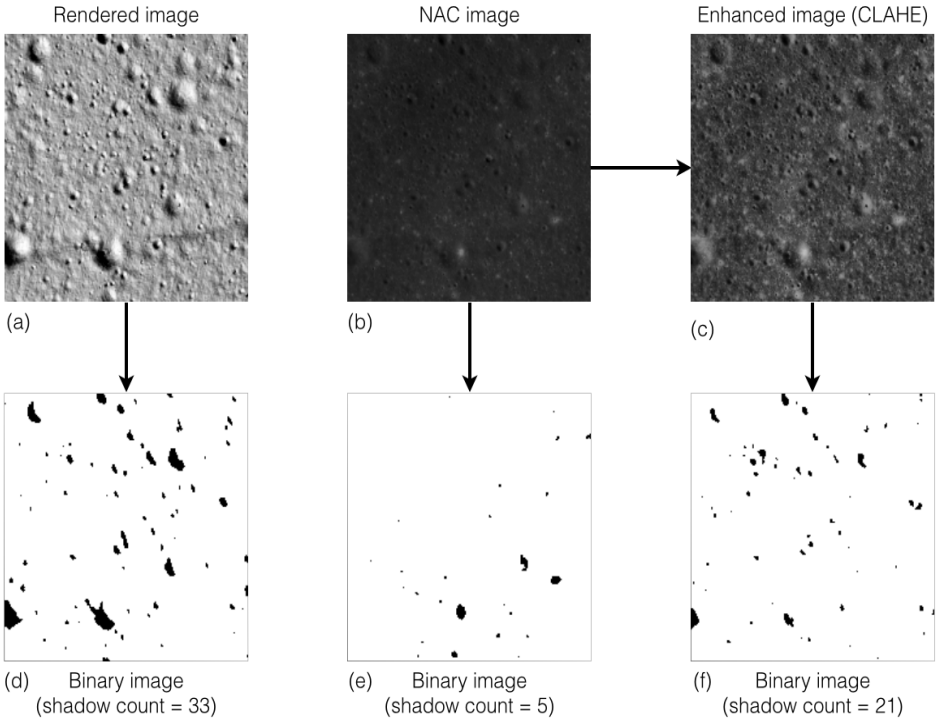

Figure 1.5: Shadow segmented rendered, NAC and enhanced images of the same mare region

Radiometric enhancement

Figure: 1.6 shows the intended use of the proposed radiometric enhancement pipeline within the BSM system. The descent image is enhanced on-board before the shadow segmentation is performed.

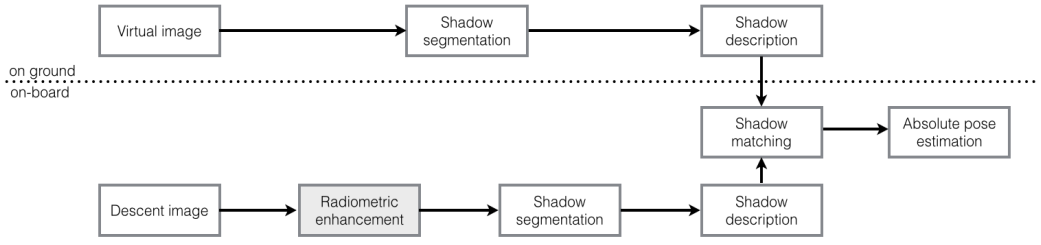

Figure 1.6: Application of the radiometric enhancement method within the BSM system

[1]the contour area is calculated using the Green's theorem [42]

As mentioned before the contrast of the images vary, due to the illumination conditions during the acquisition and due to the surface in the scene. Because of these variations in the Lunar images, it might be difficult to find one algorithm which is suitable for all images. Different images might require different enhancement algorithms to achieve the required performance of shadow segmentation.

Based on this observation, the thesis objective is divided into two parts. The first goal is the analysis of the state of art enhancement methods and check if one method is suitable for all the images with respect to shadow segmentation. If there is no unique method, then the second objective is to implement a radiometric enhancement pipeline, consisting of an image classifier and a set of suitable enhancement methods. Figure: 1.7 shows the basic structure of the radiometric enhancement pipeline. As shown, the enhancement pipeline first classifies the images subjectively based on the visual information of the scene e.g., whether the area lies in light terra region or dark mare region. After this a parametric evaluation of the image is performed, based on mathematical parameters. The values of the different mathematical parameters are used to select the suitable enhancement algorithm.

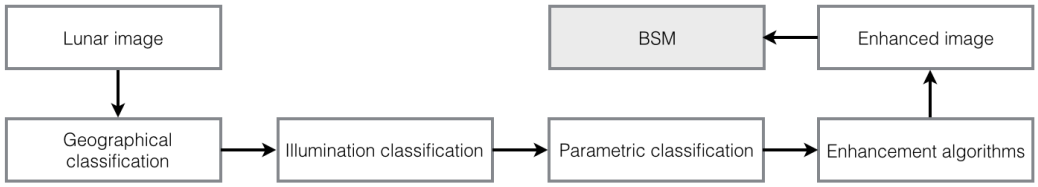

Figure 1.7: Basic structure of radiometric enhancement pipeline

This work involves analysis of available Lunar images with respect to quality, data formats and availability. The Lunar images will be classified based on scenery information of surface features and through parametric information. Based on the classification, a training data set will be created. This data set will be used to build the classification logic using the parameter value.

1.3 Methodology

To achieve the objective, the following major steps are performed:

1. Classification of scenes in Lunar images: The classification is based on scene analysis in the images (through visual inspection) and mathematical parameters.
2. Study and identify image enhancement techniques: Literature review of various available image enhancement techniques and selection of suitable techniques for Lunar image enhancement.
3. Check for unique algorithm: Out of all the enhancement algorithms identified for the enhancement, check if there is an algorithm which is applicable on all the images.

4. Set-up a pipeline of identified enhancement techniques: If a unique algorithm does not exist for all of the images, implement a classification method based on visual information and mathematical parameters.

5. Evaluation of the implemented pipeline: Evaluate the performance of the pipeline against a large data set.

1.4 Thesis overview

Chapter 2 explains the image classification methodology with examples. The third chapter discusses the state of the art image enhancement techniques investigated and an explanation of the selected algorithms. Chapter 4 describes the implementation of the pipeline. The fifth chapter describes the experimental set-up description which includes the data selection and the method used to validate the pipeline. Chapter 6 discusses the obtained results. The last chapter provides a summary of the thesis objectives and the obtained results, as well as a discussion on possible future improvements.

2 Image classification

The type of images acquired by the in-flight camera of the lander vary depending on the region of interest and the illumination conditions. The size and type (hard and soft) of the shadows depend on the *incidence angle*[1] combined with the surface morphology. Another factor affecting the shadow extraction process is the surface reflectance. Areas with low reflectance would make it difficult to differentiate between the shadows and the background. Due to variation in surface feature and the illumination condition, it is important to classify all the possible situations which might occur in a real mission. The classification of images is also important for the selection of the enhancement algorithms as one enhancement algorithm might not be applicable for all types of images. Further the classified images will be used to verify the performance of the implemented enhancement pipeline.

This chapter gives a brief introduction to shadows, followed by a detailed discussion on the classification methods used to classify the images.

Shadows

A shadow is created when an object comes between a surface and a ray of light. Shadows can be classified into two categories, hard shadows and soft shadows. Hard shadows give a binary appearance as shown in figure: 2.1, the existence of shadow is a simple yes or no question. The region of a hard shadow is well defined and there is a sharp boundary between the shadow and the illuminated region. Soft shadows on the other hand do not have a very well defined boundary and the strength of the shadow decrease radially outwards from the centre of the shadow as shown in figure: 2.2.

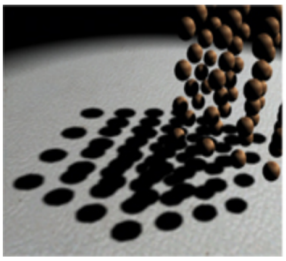

Figure 2.1: Example of hard shadow [31]

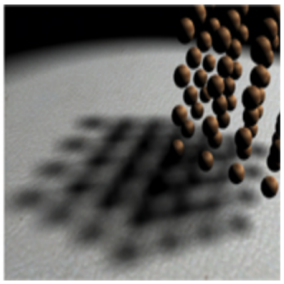

Figure 2.2: Example of soft shadow [31]

Ideally, hard shadows are created due to a point light source. Other factors such as lack of atmosphere (absence of light scattering) or presence of hard light can create shadows which are very close in appearance to hard shadows. In case of the Moon, where there is no atmosphere and hence there is no diffusion, the sun rays obstructed by craters, mountains or boulders produce strong shadows, i.e. with high contrast between the shadow and the surrounding. A hard appearance of shadow is

[1] the incidence angle is the angle between the sun and the surface normal [41]

more prominent at high incidence angle, due to low inter-reflection effect from Lunar surface.

Soft shadows are formed due to an area light source, which generates parallel light beams. Soft shadows are also the result of scattered, diffracted and inter-reflected light from an object. In case of Moon, there is no atmospheric scattering, but at low incidence angle the strength of shadows is diminished by the inter-reflectance effect.

2.1 Classification of Lunar images

Classification of scenes in Lunar images is required to select the optimal enhancement techniques to be implemented in the pipeline for automatic radiometric enhancement. The images are mainly classified based on the image brightness and topographic features in the scene. All the images considered for classification are taken from the Lunar Reconnaissance Orbiter Camera (LROC) website [44], otherwise the source is explicitly mentioned. The following major criteria has been identified for the classification of the images:

1. Visual classification: A subjective classification based on the visual inspection.
2. Parametric classification: An objective classification based on mathematical parameters such as image entropy.

2.1.1 Visual classification

The fundamental principal behind BSM is to match shadows and estimate the absolute position of the spacecraft, which makes it imperative to identify all the features responsible for shadow generation on the Lunar surface. Another factor which is important in digital image processing is the reflectance of the surface as an image is a combination of both the reflectance and the illumination. As the camera sensors convert the amount of light received to a grey value, it can happen that for dark regions the dark surface is misclassified as shadows.

The visual classification of Lunar images are based on the geographical information. As the designated landing site on the Lunar surface is known for a mission, the geographical feature information is assumed to be a prior knowledge. Based on visual analysis of NAC images and Lunar geography information provided by various sources [45, 14], images were classified based on the following:

1. Surface reflectance: The Lunar surface contains areas with both (high terra) region and (low mare) region reflectance.
2. Topography: Flat and hilly or mountainous regions on the Moon.
3. Surface feature: Depending upon the region of interest, the Lunar surface might contain craters, boulders and/or fractures.

Surface reflectance

The surface of the Moon is mainly classified into two regions based on the reflectance of the surface material. The light highland regions called terra and the dark plain regions called mare. Figure: 2.3 (section of M105795162RC[1]) shows a mare region with low surface reflectance and figure: 2.4 (section of M181495512LC) shows a terra region with high surface reflectance. This classification is important as for the darker regions, shadow segmentation is difficult under low illumination condition. Due to its limited dynamic range, the camera sensor would read similar grey level values for the shadow and the background.

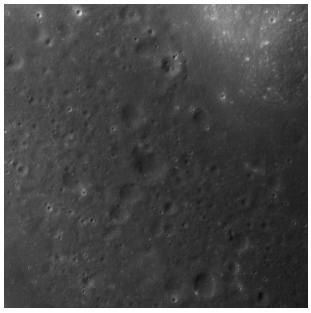

Figure 2.3: Low reflectance mare region

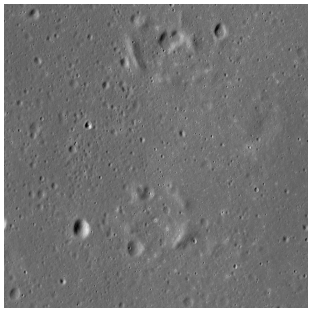

Figure 2.4: High reflectance terra region

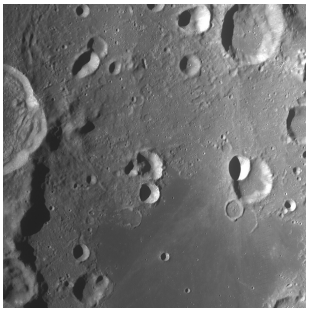

Figure 2.5: Lunar surface with mare and terra region [46]

An image of a scene containing mare and terra is challenging for the shadow segmentation process. As shown in figure: 2.5, due to low surface reflectance the mare region appears darker compared to the terra region with its high surface reflectance. In such regions the grey value acquired by the camera sensor for illuminated surface of a mare could match with the grey value of the cast shadow in the terra region.

Topography

Moon topography can be classified into two major categories, flat areas and mountainous region. The shadows in the flat surface areas are created due to the surface features such as craters. Figure: 2.6 (section of M102000149RC) shows an example of such flat region on the Moon. Depending on the surface reflectance and the illumination, the shadows due to a mountain can be large compared to crater shadows. Additionally, due to back reflectance there might be soft appearing shadows on the mountain slopes. In figure: 2.7 (section of M1123519889RC) a mountain region on the Lunar surface is shown.

[1]the numbering is the official image identifier of the LROC website [44, 2]

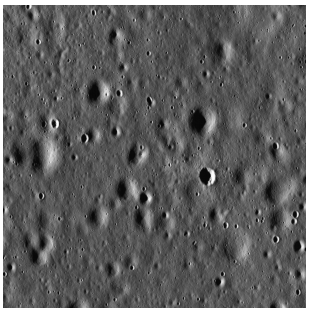

Figure 2.6: Flat area of the Lunar surface

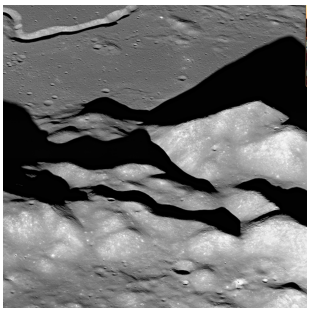

Figure 2.7: Mountain on the Lunar surface

Surface feature

The surface of the Moon has various topographic features such as craters, boulders, rilles and fractures, which can generate shadows. Craters are a robust and prominent source of shadows. Figure: 2.8 (section of M147163861LC) shows examples of crater shadows. The craters can be further classified by their age. Young craters are brighter than their surrounding and has sharp boundaries which leads to hard shadows, whereas the old craters have smooth edges which leads to soft shadows. Figure: 2.9 (section of M186056576LC) gives a comparison of young and old craters. The young crater has a distinct texture and crater ring compared to its surrounding. The bright texture of the crater, increases the dynamic range of the image, which makes the shadow segmentation process more challenging.

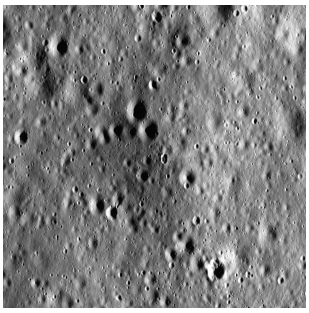

Figure 2.8: Crater on the Lunar surface

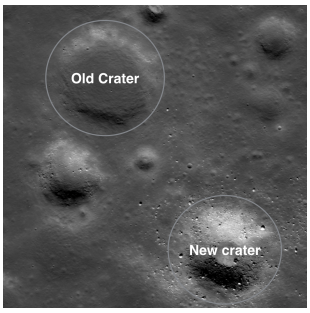

Figure 2.9: Example of young and old crater

Shadows are also generated by boulders. The size and type of the shadows depend upon the size of the boulder and the incidence angle. Figure: 2.10 (section of M187340587LRC) shows the boulders and generated shadows on the Lunar surface. Further shadows arise from fractures on the Lunar surface shown in figure 2.11 (section of M182253065RC). The shadows generated by fractures and boulders are small and it needs to be investigated if they can be used with BSM, perhaps at lower altitude, when the cast shadows appear long.

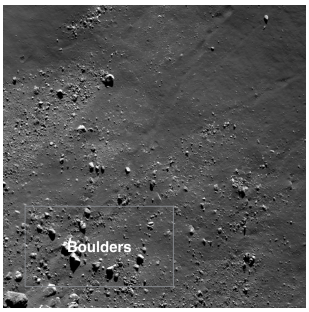

Figure 2.10: Boulders on the Lunar surface

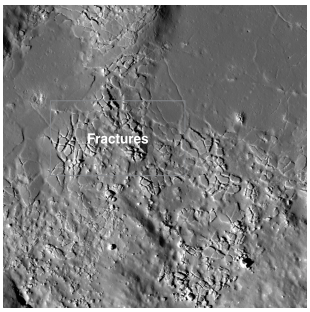

Figure 2.11: Fractures on the Lunar surface

Rilles are another prominent Lunar feature which generates shadows. The rilles can be continuous as shown in figure: 2.12 or might appear like chained craters as shown in figure: 2.13. The chained craters are considered to be undeveloped rilles [25]. The shadows generated by rilles are long and have a small width.

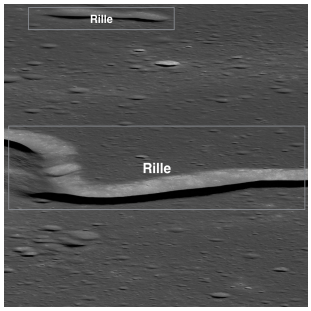

Figure 2.12: Rille on the Lunar surface

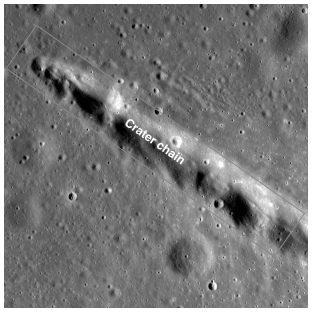

Figure 2.13: Chained craters (undeveloped rille) on the Lunar surface

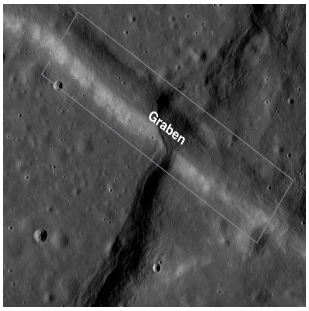

Figure 2.14: Graben on the Lunar surface

The grabens are features on Moon formed between two surface faults and downwards relative to the fault blocks, shown in figrue: 2.14. Similar to the rilles, the grabens are source of long shadows with a small width.

Figure: 2.15 shows the visual classification structure. In each classification section, it is possible to have a combination of spatial features such as craters and boulders. The first level of the classification is based on the reflectance of the surface, i.e. whether the scene belongs to the mare or the terra region. The next classification is based on the topography. The type of shadows vary based on whether the scene contains only flat surface with surface features or mountain. The shadow generated by mountains are large whereas an individual crater generates smaller shadow.

The next classification is based on the surface features, the surface of the Moon contains various shadow generating features. The strength of shadows cast by each feature, depends largely on the incidence angle and the surface reflectance. Due to rilles and graben, the cast shadow strength is high at high incidence angle, where as at relatively lower incidence angles the shadows from craters and boulders are more evident.

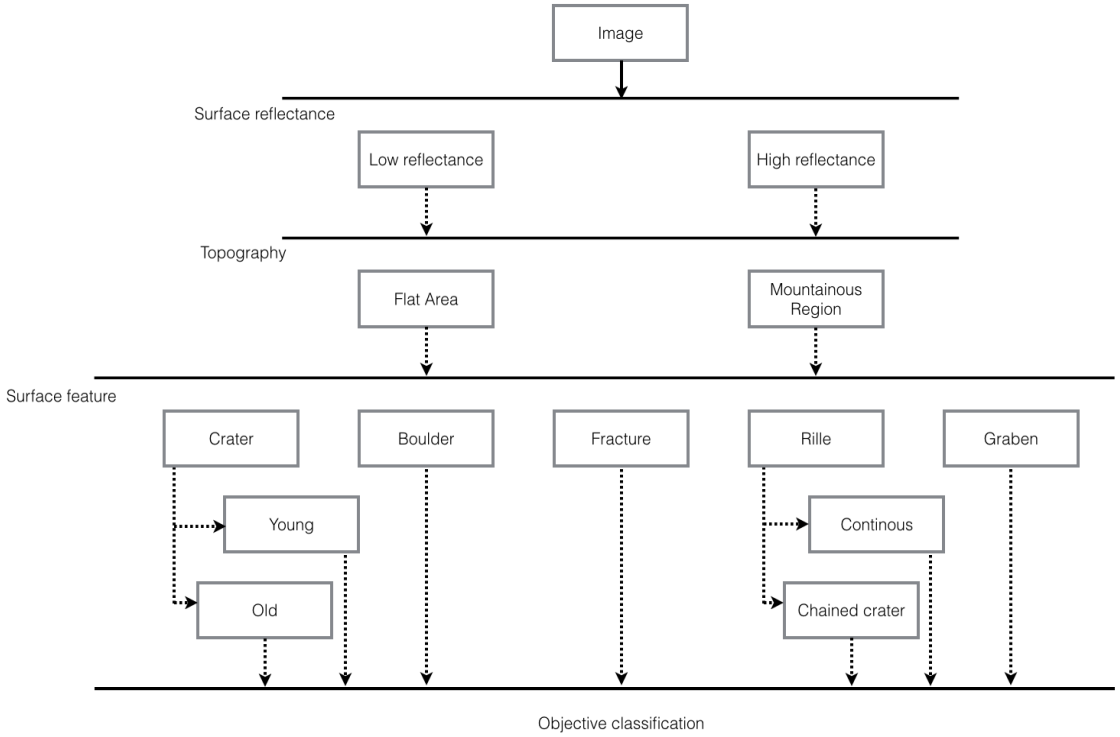

Figure 2.15: Analytical classification table

Visual classification review

In order to test the image enhancement algorithms with real images, first classification based on the classification table: 2.15 is performed. The strength of cast shadows by these features depends on the incidence angle and surface reflectance.

2.1.2 Parametric classification

The Lunar images were also classified objectively based on the following information:

1. Incidence angle: The incidence angle if based on the time of descent. It has a large influence on the shadow content of a scene.

2. Grey level co-occurrence matrix: Grey Level Co-occurrence Matrix (GLCM) is a texture based image classification method.

Incidence angle

Kaufmann et al. [18] have shown that the accuracy of a pose estimate based on the BSM decreases with a decrease in number of key points, which depends on the amount of shadows detected in the Lunar image. The size, quality (hard or soft) and direction of a shadow depends on the incident angle (time of descent). Figure: 2.16 (section of M116161085RC) and figure: 2.17 (section of M111443315RC) show the

effect of the incident angle on the same region of the Lunar surface. The images show the Apollo 11 landing site. As it can be seen the incidence angle affects the shadow information and due to reflectance also the dynamic range of the image.

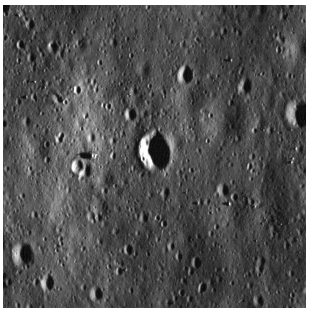

Figure 2.16: Image with incidence angle $i = 81.78^o$

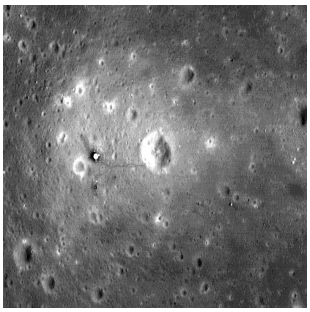

Figure 2.17: Image with incidence angle $i = 26.24^o$

Grey level co-occurrence matrix

The GLCM is a texture based image classification technique, proposed by Haralick and Shanmugam [10]. GLCM is based on the statistical information of the image for assessing the image texture. The statistics is based on the spatial relationship of the image pixels. Jia et al. [20] have used the GLCM for the analysis of Synthetic Aperture Radar (SAR) images and for urban and agricultural land classification by Umaselvi et al. [43]. Further, the GLCM has been used for the analysis of medical images by Ting and Shu [48], Mitrea et al. [22] and Mustafa et al. [22].

He and Wang [11] have proposed another texture based classification method called texture spectrum approach. In this method, the texture information is extracted from the whole 3×3 neighbourhood for each pixel. Although the method is effective, it requires huge amount of data to extract the texture, which is not available from Lunar images, hence GLCM was selected.

The GLCM was selected because of the multiple parameters which can be calculated using the GLCM matrix. Different parameters computed from GLCM, gives the measure of the image properties, hence a combination of these parameters can be used to classify the images. In this method, the frequency of a combination of grey values are stored in a matrix called grey level spatial dependence matrix.

The GLCM for an image with L levels for grey values can be computed as follows:

Decide the spatial relationship

The simplest form of the spatial relationship is the selection of the neighbour pixel next to the reference pixel in horizontal direction for each row, from left to right. The neighbour pixel can also be selected with a gap of n pixels. Based on the desired texture information, the neighbour pixel can also be selected in the vertical direction or at a desired angle. For table: 2.1, the GLCM matrix is created for the horizontal direction and the neighbour pixel is the immediate next to the reference pixel.

Build the matrix

To explain the GLCM matrix an image with a depth of 2 bit and a resolution of 4×4 is selected, as shown in table: 2.1. The GLCM matrix of this image is shown in table: 2.2. For the image the relation of 0 as reference pixel and 1 as neighbouring pixel occurs 3 times, hence the row with grey value 0 and column with grey value 1 of GLCM shown in table: 2.2 is updated with 3. It is important to note that the GLCM matrix is horizontal, from left to right and for each row.

0	1	2	0
1	0	1	2
3	0	1	2
1	3	2	0

Table 2.1: Example image with depth of 2 bits

	0	1	2	3
0	0	3	0	0
1	1	0	3	1
2	2	0	0	0
3	1	0	1	0

Table 2.2: GLCM matrix of table: 2.1

Based on above example the general form of GLCM horizontal matrix M_G is shown in table: 2.3.

	0	1	2	$\cdots$	L-2	L-1
0	0,0	0,1	0,2	$\cdots$	0,L-2	0,L-1
1	1,0	1,1	1,2	$\cdots$	1,L-2	1,L-1
2	2,0	2,1	2,2	$\cdots$	2,L-2	2,L-1
$\vdots$	$\vdots$	$\vdots$	$\vdots$	$\ddots$	$\vdots$	$\vdots$
L-2	L-2,0	L-2,1	L-2,2	$\cdots$	L-2,L-2	L-2,L-1
L-1	L-1,0	L-1,1	L-1,2	$\cdots$	L-1,L-2	L-1,L-1

Table 2.3: GLCM matrix

Make the matrix symmetrical

To make the matrix symmetrical the horizontal build up has to be repeated for the vertical direction, which can be achieved by transposing the matrix and add the transposed matrix with the original matrix as given in equation: 2.1

$$V = M_G + M_G^{'} \tag{2.1}$$

where, V is the symmetrical GLCM matrix.

Normalize the matrix

Normalise the GLCM matrix using the equation: 2.2.

$$P_v(i,j) = \frac{V(i,j)}{\sum_{i,j=0}^{N-1} V(i,j))} \tag{2.2}$$

where, $P_v(i,j)$ is the normalised value at (x,y). The parameters which can be calculated from the GLCM matrix are GLCM contrast, GLCM correlation, GLCM energy, GLCM entropy, GLCM dissimilarity, GLCM homogeneity, GLCM mean and GLCM variance for image analysis and classification.

A combination of three parameters namely contrast, correlation and entropy (of GLCM) were used to classify the Lunar image. The selection of the aforementioned parameters computed from the GLCM matrix are considered based on the results discussed by Clausi [5]. In his research the author found that the combination of contrast, correlation and entropy outperforms a combination of all other measures (such as energy, dissimilarity, etc.).

GLCM Contrast

GLCM contrast $cont_v$ is calculated as shown in equation: 2.3. A GLCM contrast value of 0 means that the image contains only one grey level and hence has no contrast. Though the maximum value of the GLCM contrast depends on the size of the GLCM matrix, for a given matrix size, higher value would represent higher contrast level in the image.

$$cont_v = \sum_{i,j=0}^{N-1} P_v(i,j)(i-j)^2 \tag{2.3}$$

GLCM correlation

The calculation of GLCM correlation $corr_v$ value is based on the mean and standard deviation, as shown by equation: 2.4e. GLCM correlation provides the linear dependency of a pixel value with neighbouring pixels. A value of 0 means that the pixels are uncorrelated and a value of 1 means perfect correlation.

$$\mu(i) = \sum_{i,j=0}^{N-1} iP_v(i,j) \tag{2.4a}$$

$$\mu(j) = \sum_{i,j=0}^{N-1} jP_v(i,j) \tag{2.4b}$$

$$\sigma(i)^2 = \sum_{i,j=0}^{N-1} (i-\mu(i))P_v(i,j) \tag{2.4c}$$

$$\sigma(j)^2 = \sum_{i,j=0}^{N-1} (j-\mu(i))P_v(i,j) \tag{2.4d}$$

$$corr_v = \sum_{i,j=0}^{N-1} P_v(i,j)[\frac{(i-\mu(i))(j-\mu(j))}{\sqrt{(\sigma(i)^2)(\sigma(j)^2)}}] \tag{2.4e}$$

GLCM Entropy

The computation of GLCM entropy is similar to image entropy with the change of natural log. GLCM entropy h_v computation is shown in equation: 2.5. The

GLCM entropy tells the uniformity of the contrast level of the GLCM matrix, this information also varies from image to image and is related with the image entropy. If the grey level distribution in the image is even, the value of the GLCM entropy is maximum.

$$h_v = \sum_{i,j=0}^{L-1} p_v(i,j)(-\log p_v(i,j)) \tag{2.5}$$

In addition to parameters computed from GLCM matrix, Image entropy was also considered for classification.

Image entropy

Entropy is a measure of randomness, and an image of high randomness means that the histogram is evenly equalised. The value of image entropy provides the average information content of the image. The formula to calculate image entropy H discussed by Gonzalez and Woods [9] [page: 263] in bits is given by equation 2.6.

$$H = -\sum_{i=0}^{i=L-1} p(i)\log_2 p(i) \tag{2.6}$$

where L is the number of grey levels, $p(i)$ is the probability of grey level i. Entropy in thermodynamics gives the randomness measure of the system. In image processing, the entropy value provides the amount of information contained by the image. The minimum amount of information contained by the image is 0 when all the grey pixels have the same value. The maximum entropy value for an image (of depth 8) is 8, when the occurrence probability of all the grey values between 0 to $L-1$ is the same.

Classification structure

Figure: 2.18 shows the objective classification structure. The image is classified based on the incidence angle, GLCM entropy, GLCM contrast, GLCM correlation and image entropy. Based on the value of these parameters, the enhancement algorithm is selected.

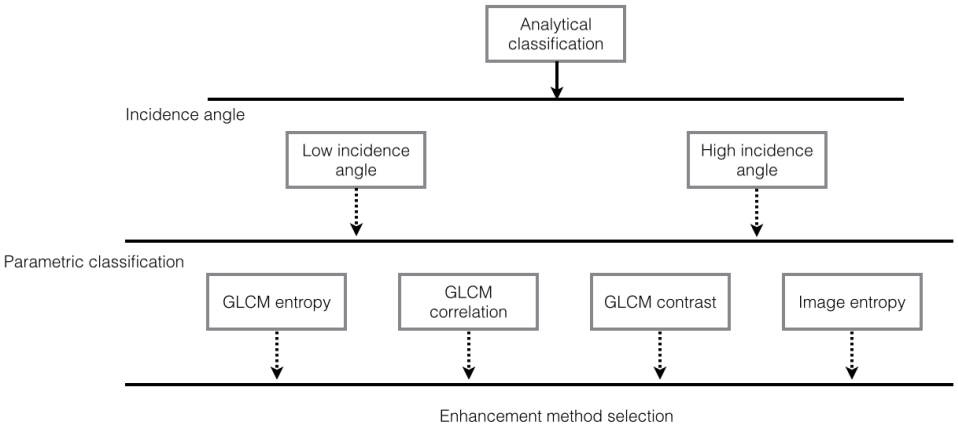

Figure 2.18: Objective classification table

Parametric classification review

Parametric classification is based on the image acquisition conditions of the image and the information content of the image. As discussed earlier, the incidence angle affects the strength of shadows. And the incidence angle depends on the image acquisition time. Next the image is classified based on the contrast, entropy and correlation calculated from the GLCM matrix and the image entropy.

Parametric classification is proposed for the second objective, that is if there is no unique algorithm which is applicable on all the images. A relation between the different parameters and the enhancement algorithm can be established based on a sample execution. And this relation can be used to select the applicable algorithm based on the parameter values of an image.

3 Radiometric enhancement methods

This chapter investigates the state of the art image of enhancement methods. The focus is on methods which provide contrast enhancement for grey scale images. It is assumed that the landing spacecraft will be equipped with a monochrome camera, which provides grey scale images.

As discussed in the previous chapter, Lunar images vary largely in brightness and texture, which means one enhancement method might not provide desired result for all images under-consideration. Based on the global and local brightness level and texture information the radiometric enhancement pipeline has to include different enhancement algorithms. Sanchez and Canton [36] [chapter: 9] have classified space image processing primarily into two groups, spatial domain methods and frequency domain methods.

3.1 Spatial domain processing

In spatial domain methods pixels are directly manipulated. The spatial domain is based on pixel level mapping, where the mapping function is based on the selected enhancement method. The spatial domain methods can be further divided into two major categories point processing techniques and mask processing techniques. These two methods are discussed in detail in the next sections.

3.1.1 Point processing methods

In point processing methods, the input pixel value is computed solely based on that pixel's value. The point processing methods are simple and efficient techniques for radiometric image enhancement. Point based methods are mainly used for contrast enhancement and colour value modification for coloured images, improving the image quality subjectively. As an individual pixel is modified for enhancement, the methods fails to remove noise or perform segmentation, for noise reduction and segmentation mask based processing techniques are used.

Based on mathematical functions

Image Negatives (IN) [9] [page: 130] can be used to view the relatively small bright or grey regions in an image with dominant dark areas. Log Transformation (LT) [23] [page: 48] can be used to compress the dynamic range of the images for display. Gonzalez and Woods [9] [page: 131] have shown the effect of dynamic range compression using the Fourier Transform (FT). Images can also be enhanced based on a piecewise transformation called contrast stretching, where the range of the pixel values are divided into sub-sets and each subset is mapped using a different mapping [9] [page: 137]. To highlight a particular region in the image, another piecewise linear transformation called grey level slicing[1] [9] [page: 137] can be used.

[1] also known as intensity level slicing

Power Law Transforms (PLT)[1] [9] [page: 132], can be used to both increase or decrease the dynamic range of the images. Scott and Pusateri [38] have proposed an automatic method to select the value of gamma based on the statistical information of the image for hardware implementation. However, their implementation uses the information from the previous frame to calculate the gamma value to be used for the correction of the current frame, which is applicable only in video enhancement as the information change from one frame to another is assumed to be very low. A localised gamma correction is proposed by Qiao and Ng [34], where the gamma value is updated based on the local statistics of the image. The method calculates the weight for the current kernel, and the computed weight is used to adjust the gamma value. The benefit of using this method is that the pixels of dark regions are enhanced more than the ones in bright regions. However gamma correction is applied for display systems and it controls the brightness of the image, not the contrast.

Based on the histogram of the image

Histogram Matching (HM) [9] [page: 150] is a technique in which the histogram of the input image is matched with the user defined histogram. The disadvantage of this method is that it is not adaptable and for each image based on the information content or application a desired output histogram has to be specified. As the scene information during the descent phase is assumed to be dynamic, fixing a predefined output histogram was not considered to be an efficient solution.

Histogram Equalization (HE) [9] [page: 144], utilises the Cumulative Distribution Function (CDF) to map the grey levels from the original image to the grey levels of the enhanced image. Although, HE is computationally very efficient, the performance of the method is limited to low dynamic range images. HE of high dynamic range images results in intensity saturation and amplification of noise. HE was selected to test its performance on images with low contrast. The algorithm of HE is discussed in section: 3.3.1.

To balance the effect of localised bright and dark regions in HE, Adaptive Histogram Equalization (AHE)[2] was proposed for cockpit displays by Ketcham et al. [19]. The AHE is a non-linear method, where the local statistics of the image is used to adaptively compute the grey level value. Although this method is very effective in image enhancement, it is computationally very expensive. To reduce the computational requirement Pizer et al. [32] have proposed a sampling and interpolation method to speed up the basic form of AHE. Another method to improve the speed of AHE is proposed by Zhiming and Jianhua [49] for hardware implementation. By using a combination of an iterative sliding window (for histogram calculation) and a bit wise shift (to speed up the multiplication and the division process), a speed-up of 98.1% over AHE (for window size of 128 and depth of 8 bit) was achieved. Based on its capability to equalise the local areas evenly, AHE was selected for enhancing images with high dynamic range. The AHE algorithm is explained in detail in section: 3.3.2.

[1] also known as Gamma Correction (GC)

[2] the authors in the document have used the term Local Area Histogram Equalization (LAHE) for AHE.

The AHE in general produces good results for high dynamic range images, but as discussed by Pizer et al. [32], it also enhances the noise. The noise amplification is high in a homogeneous neighbourhood, where the transformation applied maps the narrow pixel range to whole range of the image, over amplifying the noise. To prevent this, CLAHE was proposed by Pizer et al. [32].

In CLAHE an individual histogram of each region is clipped using a clipping limit. The clipped region is then redistributed to the neighbourhood and the same process is iterated until an acceptable excess value is achieved. CLAHE was selected for images with high dynamic ranges, with the advantage of the clip limit, the enhanced images can avoid high output dynamic range, which should be suitable for the adaptive shadow segmentation method. More about the CLAHE algorithm is discussed in section: 3.3.3.

Singh and Kapoor [39] have proposed an exposure based sub-image histogram equalisation technique. The image is divided into two sub images of different intensities and to avoid saturation the histograms are also clipped using a clip limit as the average value of the grey level. The two sub-images are enhanced individually and combined to get the enhanced image. This method was selected for Lunar image enhancement as it increases the contrast of low exposure images. This algorithm is explained in detail in section: 3.3.4.

Other point based techniques such as image subtraction is used in robotics [7] for target tracking (by subtracting the background) and to observe asteroids [8], by removing the static objects in the background. Subtracting two consecutive images makes it easier to track a moving object (or multiple moving objects) in a cluttered background. Image averaging is used to remove uncorrelated noise with zero mean value. It is very often used to enhance the image quality of a distant galaxy as discussed by Sanchez and Canton [37]. Aforementioned methods were not selected, as these methods are not suitable for image contrast enhancement.

3.1.2 Mask processing methods

In mask processing methods, the enhanced pixel value is computed from the input pixel value and the values of neighbouring pixels using a Spatial Filter (SF). The spatial filters are selected based on the desired operation to be performed on the image.

The mean and median filters are used to remove noise as discussed by Moeslund [23] [page: 71], some spatial filters are used to detect geometrical shapes in the image (such as Hough transform for circle detection).

Another important field of spatial filtering is morphology as discussed by Pratt [33] which is mainly used in binary images to increase the size (dilution) [page: 455] or reduce the size of an object (erosion) [page:457].

Template matching is used to locate an object in the image as discussed by Moeslund [23] [page: 78]. Huihui et al. [40] have proposed the shadow segmentation of coloured

images through the template matching approach.

The two fundamental operations used in mask processing methods are convolution and correlation.

$$g(i,j) = \sum_{k=-n/2}^{k=n/2} \sum_{l=-n/2}^{l=n/2} h(k,l) f(i-k, j-l) \tag{3.1}$$

The convolution operation represented by equation: 3.1 is used for image smoothing or noise filtering where as the correlation operation shown in equation: 3.2 is used for template matching.

$$g(i,j) = \sum_{k=-n/2}^{k=n/2} \sum_{l=-n/2}^{l=n/2} h(k,l) f(i+k, j+l) \tag{3.2}$$

Mask processing methods were not investigated further as the focus of this thesis is on contrast enhancement of the image, not on noise reduction or object detection.

3.2 Frequency domain processing

In frequency domain processing the Discrete Fourier Transform (DFT) of the image is modified (using frequency domain filter). The enhanced image is obtained by taking the Inverse Discrete Fourier Transform (IDFT) of the modified DFT as discussed by Gonzalez and Woods [9] [chapter: 4]. The DFT of the image $f(x, y)$ is calculated as shown in equation: 3.3.

$$F(u,v) = \sum_{i=0}^{i=M-1} \sum_{j=0}^{j=N-1} f(i,j) \exp^{-j2\pi(ui/M + vj/N)} \tag{3.3}$$

Considering the DFT of filter $h(x, y)$ to be $H(u, v)$, the processed DFT of the image $G(u, v)$ is given by equation:3.4.

$$G(u,v) = H(u,v) \times F(u,v) \tag{3.4}$$

The IDFT is calculated using the equation: 3.5

$$g(i,j) = \sum_{i=0}^{i=M-1} \sum_{j=0}^{j=N-1} G(u,v) \exp^{-j2\pi(ui/M + vj/N)} \tag{3.5}$$

Frequency domain filtering, when used for image smoothing and image sharpening are computationally very efficient compared to spatial domain filtering as the convolution in spatial domain is only a multiplication in frequency domain.

One of the important filtering methods in frequency domain is called Homomorphic Filtering (HF) discussed by Gonzalez and Woods [9] [page: 185]. The advantage of such a filtering technique is in suppressing the effect of uneven low frequency

illumination by applying a high pass filter. The homomorphic filtering is based on the fact that an image is a combination of two factors, illumination $i(k,l)$ (the low frequency component) and reflectance $r(k,l)$ (the high frequency component) as shown in equation: 3.6.

$$f(k,l) = r(k,l) \times i(k,l) \tag{3.6}$$

Section: 3.3.5 explains the homomorphic filtering in detail.

3.3 Selected algorithms

As the objective is to detect shadows in the descent image after the enhancement, the methods are studied with the main focus on their enhancement capabilities in terms of contrast. So that the shadow segmentation can be robust and reliable. During image classification, as mentioned in chapter: 2, it was observed that the images vary mainly in contrast level. In some of the images, localised low exposed regions were observed. Uneven illumination in the images is another issue in the images, which makes some of the areas much brighter than the rest. These variations in the image affect the adaptive threshold selection for shadow segmentation, leading to false detection or rejection of shadows. Among the various algorithms for image enhancement, the algorithms were selected based on the following capabilities:

1. Contrast improvement at global level: The algorithm is capable to enhance the global contrast of the image (applicable for low dynamic range images).
2. Contrast improvement at local level: The algorithm is capable to enhance the local contrast of the image (applicable for images with localised brightness or high dynamic range).
3. Capability to equalise the uneven illumination: The algorithm is capable to filter the illumination (Some of the images were found to have bright areas, due to illumination).
4. Capability to enhance low exposed areas: The algorithm is capable to enhance the low exposure areas.
5. Capability to avoid grey level saturation: During the enhancement, the algorithm is capable of preventing the *saturation effect*[1] in the image.
6. Adaptive across images: The algorithm is adaptable and enhances the image at local and global level.

The level of improvement in contrast is important for the shadow segmentation, as the contrast level in the image decides the dynamic range of the image, which in turn affects the shadow thresholding value. Very high contrast levels might lead to

[1] the image pixels have minimum or maximum grey value, which makes some regions in the image darker or brighter than desired

false shadow detection and very low contrast level might miss some of the actual shadows. Hence, it is critical to enhance the images with the optimal contrast for the desired results. The state of the art of image enhancement algorithms and their properties are listed in table: 3.1.

	LT	GC	HE	AHE	CLAHE	ESIHE	SF	HF
Contrast improvement at global level	×	×	✓	✓	✓	✓	×	✓
Contrast improvement at local level	×	×	×	✓	✓	✓	×	×
Capability to equalise the uneven illumination	×	×	✓	×	×	×	×	✓
Capability to enhance low exposed areas	×	×	✓	✓	✓	✓	×	×
Capability to avoid grey level saturation	×	×	×	×	✓	✓	×	✓
Adaptive across images	×	×	×	×	✓	✓	×	×
Selected	×	×	✓	✓	✓	✓	×	✓

IN: Image Negative, LT: Logarithmic Transform, GC: Gamma Correction, HE: Histogram Equalisation
AHE: Adaptive Histogram Equalisation, CLAHE: Contrast Limited Histogram Equalisation
ESIHE: Exposure based Sub-Image Histogram Equalisation, SF: Spatial Filtering, HF: Homomorphic Filtering

Table 3.1: Algorithm selection matrix,

The algorithms were selected based on the following justification:

1. Histogram equalisation: Expected to work well on images with low dynamic range.
2. Adaptive histogram equalisation: Expected to work well on images with high dynamic range.
3. Contrast limited histogram equalisation: Expected to work on images with high dynamic range and to avoid the saturation effect.
4. Exposure based sub-image histogram equalisation: Expected to work well on images with low and high exposure areas.
5. Homomorphic filtering: Expected to normalise the brightness in the image.

In the following, the selected algorithms are explained in more detail to provide a deeper understanding for the implemented and tested methods.

3.3.1 Histogram equalisation

HE is a contrast adjustment technique for images with low dynamic range. The normalised histogram (also the probability distribution) is given by equation: 3.7.

$$p(k) = \frac{n_k}{n} \tag{3.7}$$

where, $p(k)$ is the probability of the occurrence of grey level value k, n_k is the total number of pixels with value k, n is the total number of pixels in the image and

$k = 0, 1, 2, ..., L-1$. L is the grey level values. The new pixel value is computed based on the CDF of the normalised histogram described in equation: 3.8 and 3.9.

$$c_k = \sum_{j=0}^{k} p(j) = \sum_{j=0}^{k} \frac{n_j}{n} \tag{3.8}$$

$$g_k = (L-1) \times c_k \tag{3.9}$$

where, c_k is the CDF from 0 to the input grey level k and g_k is the new pixel value. The HE is summarised in algorithm: 1.

Algorithm 1 Histogram equalisation

```
for i ← 0, M − 1 do                    → histogram
    for j ← 0, N − 1 do
        n(f(i, j)) ← n(f(i, j)) + 1
    end for
end for
for k ← 0, L − 1 do                    → probability distribution
    p(k) ← n(k)/(M × N)
end for
c(0) ← p(0)
for k ← 1, L − 1 do                    → cumulative distribution
    c(k) ← c(k − 1) + p(k)
end for
for k ← 0, L − 1 do                    → lookup table
    t(k) ← c(k) × (L − 1)
end for
for i ← 0, M − 1 do                    → enhanced image
    for j ← 0, N − 1 do
        g(i, j) ← t(f(i, j))
    end for
end for
```

3.3.2 Adaptive histogram equalisation

To reduce the computational overload of the original AHE by Ketcham et al. [19], Pizer et al. [32] proposed a sampling and interpolation method to perform AHE, which is also used in this thesis.

In the proposed method an image is divided into equally sized rectangular tiles (typically $W \times W$). A CDF is computed for each tile, shown in the left part of Figure: 3.1. The green region is bi-linearly interpolated using the CDF of the four region, the orange region is linearly interpolated and the blue region is transformed with the corner tile CDF.

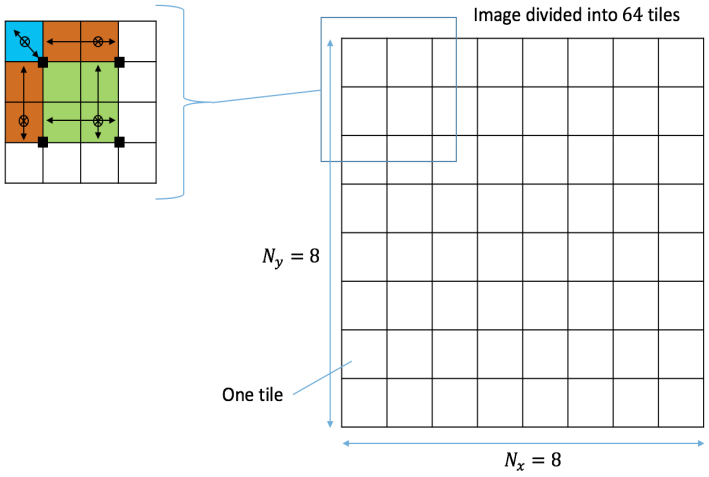

Figure 3.1: Tile based AHE: sampling and interpolation [19]

The linear interpolation is achieved by:

$$m_l = \frac{x_2 - x}{x_2 - x_1} m_{11} + \frac{x - x_1}{x_2 - x_1} m_{21} \tag{3.10}$$

The bilinear interpolation is achieved by:

$$\begin{aligned} m_b = \frac{1}{(x_2 - x_1)(y_2 - y_1)} & (m_{11}(x_2 - x)(y_2 - y) + \\ & (m_{21}(x - x_1)(y_2 - y) + \\ & (m_{12}(x_2 - x)(y - y_1) + \\ & (m_{22}(x - x_1)(y - y_1)) \end{aligned} \tag{3.11}$$

In equation: 3.10, m_l is the linearly interpolated new intensity value of the pixel at location (x, y) for the orange region. In equation: 3.11 m_b is the bi-linearly interpolated new intensity value of the pixel at location (x, y) for the green region, m_{11} is the mapped intensity of the upper left tile centre at position (x_1, y_1), m_{21} is the mapped intensity of the upper right tile centre at position (x_2, y_1), m_{12} is the mapped intensity of the lower left tile centre at position (x_1, y_2), m_{22} is the mapped intensity of the lower right tile centre at position (x_2, y_2).

Using algorithm: 2, the image is divided into multiple tiles. For each tile the CDF and lookup table is calculated. $P \times Q$ gives the total number of tiles. m and n are the number of rows and columns respectively for each tile. f_{xy} represents an individual tile.

Algorithm 2 Adaptive histogram equalisation: part 1

$m \leftarrow M/P$
$n \leftarrow N/Q$
for $x \leftarrow 0, P-1$ **do** $\rightarrow$ tile and lookup table
  for $y \leftarrow 0, Q-1$ **do**
    $f_{xy} \leftarrow f[m \times x : (m \times (x+1)) - 1, n \times y : (n \times (y+1)) - 1]$
    for $r \leftarrow 0, m-1$ **do** $\rightarrow$ histogram for each tile
      for $c \leftarrow 0, n-1$ **do**
        $n_{xy}(f_{xy}(r,c)) \leftarrow n_{xy}(f_{xy}(r,c)) + 1$
      end for
    end for
    for $k \leftarrow 0, L-1$ **do** $\rightarrow$ probability distribution for each tile
      $p_{xy}(k) \leftarrow n_{xy}(k)/(m \times n)$
    end for
    $c_{xy}(0) \leftarrow p_{xy}(0)$
    for $k \leftarrow 1, L-1$ **do** $\rightarrow$ cumulative distribution for each tile
      $c_{xy}(k) \leftarrow c_{xy}(k-1) + p_{xy}(k)$
    end for
    for $k \leftarrow 0, L-1$ **do** $\rightarrow$ lookup table for each tile
      $t_{xy}(k) \leftarrow c_{xy}(k) \times (L-1)$
    end for
  end for
end for

For interpolation the method proposed by Zuiderveld [50] is used in algorithm: 3. This method was selected instead of the method proposed by Pizer et al. [32], as the method by Zuiderveld is computationally more efficient. $R()$ represents the region as shown in figure: 3.2. The region classification is shown in figure: 3.1.

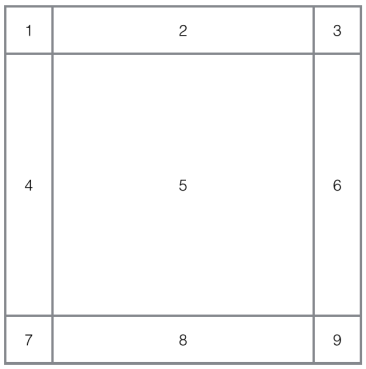

Figure 3.2: Region classification for interpolation [19]

Region $1, 3, 7, 8$ are the corner regions which are enhanced with the CDF of respective tiles. Regions $2, 4, 6, 8$ are enhanced using the linear interpolation and the region 5 is enhanced using the bi-linear interpolation.

Algorithm 3 Adaptive histogram equalisation: part 2

for $i \leftarrow 0, M-1$ **do**
  for $j \leftarrow 0, N-1$ **do**
    $x \leftarrow \lfloor i/m \rfloor$
    $y \leftarrow \lfloor j/n \rfloor$
    if $(i,j) \in R(1,3,7,9)$ **then** → map corners
      $g(i,j) = t_{xy}(f(i,j))$
    end if
    if $(i,j) \in R(2,8)$ **then** → map horizontal border regions
      $y \leftarrow (j - \lfloor n/2 \rfloor)/n$
      if $(i,j) \in R(8)$ **then**
        $x \leftarrow P-1$
      end if
      $w_1 \leftarrow ((j - \lfloor n/2 \rfloor)\%n)/n$
      $w_2 \leftarrow 1 - w_1$
      $g(i,j) \leftarrow uint8(t_{xy}(f(i,j)) \times w_2 + t_{x(y+1)}(f(i,j)) \times w_1)$
    end if
    if $(i,j) \in R(4,6)$ **then** → map vertical border regions
      $x \leftarrow (i - \lfloor m/2 \rfloor)/m$
      if $(i,j) \in R(6)$ **then**
        $y \leftarrow Q-1$
      end if
      $w_1 \leftarrow ((i - \lfloor m/2 \rfloor)\%m)/m$
      $w_2 \leftarrow 1 - w_1$
      $g(i,j) \leftarrow uint8(t_{xy}(f(i,j)) \times w_2 + t_{(x+1)y}(f(i,j)) \times w_1)$
    end if
    if $(i,j) \in R(5)$ **then** → map the centre region
      $y \leftarrow (j - \lfloor n/2 \rfloor)/n$
      $x \leftarrow (i - \lfloor m/2 \rfloor)/m$
      $w_1 \leftarrow ((j - \lfloor n/2 \rfloor)\%n)/n$
      $w_2 \leftarrow 1 - w_1$
      $w_3 \leftarrow ((i - \lfloor m/2 \rfloor)\%m)/m$
      $w_4 \leftarrow 1 - w_3$
      $g(i,j) \leftarrow uint8(w_4 \times (t_{xy}(f(i,j)) \times w_2 + t_{(x+1)y}(f(i,j)) \times w_1))$
        $+w_3 \times (t_{x(y+1)}(f(i,j)) \times w_2 + t_{(x+1)(y+1)}(f(i,j)) \times w_1))$
    end if
  end for
end for

3.3.3 Contrast limited adaptive histogram equalisation

AHE in general produces good results, but it also enhances the noise as discussed by Pizer et al. [32]. The noise amplification is high in homogeneous neighbourhood, where the applied transformation maps the narrow pixel range to the whole range of

the image. To prevent this, CLAHE was proposed by Pizer et al. [32] and Zuiderveld [50]. The author has proposed to set a maximum value for the count of each grey level in the histogram, the clipped region is then redistributed to the neighbourhood and the same process is iterated until an acceptable excess value is achieved. Figure: 3.3 shows the working principal of CLAHE.

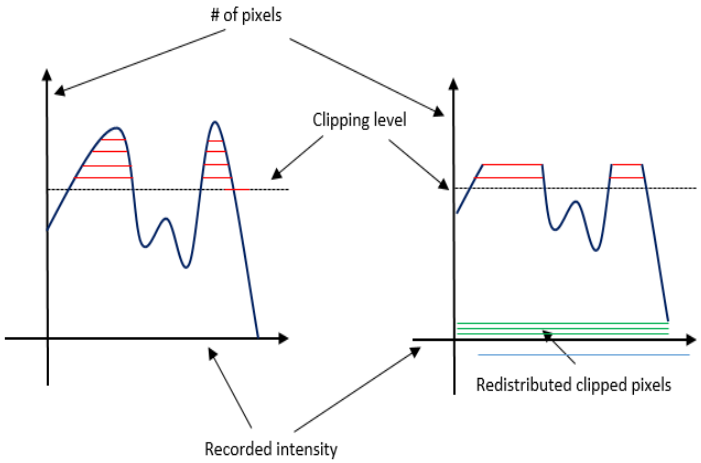

Figure 3.3: Working principle of CLAHE [32]

Pizer et al. [32] have proposed the binary search method to select the clipping limit. Another method of adaptive clip limit selection is proposed by Bhat and Tarun [1], using a least mean square algorithm. For the the implementation, the method proposed by Jintasuttisak and Intajag [12] is used. The selected method is efficient as it does not require multiple iterations as proposed by Pizer at al. or complex computation as proposed by Bhat and Tarun. Moreover after the clipping there is no overshoot in the histogram (as is the case in the method proposed by Pizer et al.). The clip limit calculation is corrected for the loss of clipped values due to non-adaptive averaging.

Since the only difference between the AHE and the CLAHE is the clipping of the histogram, only the algorithm to calculate the clip-limit is discussed in algorithm: 4. In algorithm: 4, A is the average bin content, T is the clip threshold, c is the clip value between [0,1] set by user, δ is the summation of clipped values, δ_a is the average of clipped values, N_b is the number of bins which are not clipped.

Algorithm 4 CLAHE (clip-limit)

$A \leftarrow \lfloor (m \times n)/L \rfloor$ → average pixel to each bin
$T \leftarrow A + \lfloor c \times (m \times n - A) \rfloor$ → threshold
$\delta \leftarrow 0$
$N_b \leftarrow L$
for $k \leftarrow 0, L-1$ **do** → store the clipped values
  if $n_{xy}(k) > T$ **then**
    $\delta \leftarrow \delta + n_{xy}(k) - T$
    $N_b \leftarrow N_b - 1$
  end if
end for
$\delta_a \leftarrow \lfloor \delta / N_b \rfloor$ → distribute the clipped value to each bin
for $k \leftarrow 0, L-1$ **do** → set the threshold in histogram
  if $n_{xy}(k) > T$ **then**
    $n_{xy}(k) \leftarrow T$
  else if $n_{xy}(k) + \delta_a > T$ **then**
    $n_{xy}(k) \leftarrow T$
    $\delta \leftarrow \delta - (T - n_{xy}(k))$ → remove the used clipped values
    $N_b \leftarrow N_b - 1$ → remove adjusted bins
  end if
end for
$\delta_a \leftarrow \lfloor \delta / N_b \rfloor$
for $k \leftarrow 0, L-1$ **do** → redistribute the clipped values
  if $n_{xy}(k) < T$ **then**
    $n_{xy}(k) \leftarrow n_{xy}(k) + \delta_a$
  end if
end for

3.3.4 Exposure based sub-image histogram equalization

Proposed by Singh and Kapoor [39] for grey scale images, ESIHE works well for low exposure region contrast enhancement. To avoid saturation the histogram is clipped and divided into two sub-histograms based on the exposure level. Each sub histogram is equalised individually and combined to obtain the enhanced image. The underexposed sub-histogram is compensated by increasing the count of higher grey level values. The grey level count for overexposed regions is reduced by clipping the histogram. Algorithm: 5 explains the implementation of ESIHE.

Algorithm 5 Exposure based sub-image histogram equalization: part 1

for $i \leftarrow 0, M-1$ **do** → histogram
  for $j \leftarrow 0, N-1$ **do**
    $n(f(i,j)) \leftarrow n(f(i,j)) + 1$
  end for
end for
$E_v \leftarrow \frac{1}{L} \frac{\sum_{k=0}^{L-1} n(k)k}{\sum_{k=0}^{L-1} n(k)}$ → exposure
$c \leftarrow \frac{1}{L} \sum_{k=0}^{L-1} n(k)$ → clip-limit
for $j \leftarrow 0, L-1$ **do** → apply clip-limit
  if n(k)>c **then**
    $n(k) \leftarrow c$
  end if
end for
$X_a \leftarrow L(1 - E_v)$
$n_u(k) \leftarrow n[0 : X_a]$ → separate the histogram
$n_o(k) \leftarrow n[X_a + 1 : L - 1]$

The calculated CDF of the underexposed sub-histogram $n_u(k)$ is $c_u(k)$ and for the overexposed sub-histogram $n_o(k)$ is $c_0(k)$, the enhanced image is computed based on algorithm: 6

Algorithm 6 Exposure based sub-image histogram equalization: part 2

for $i \leftarrow 0, M-1$ **do** → combine the two histograms
  for $j \leftarrow 0, N-1$ **do**
    if $f(i,j) \leq L(1 - E_v)$ **then**
      $g(i,j) \leftarrow X_a \times c_u(f(i,j))$
    else
      $g(i,j) \leftarrow (X_a + 1) + (L - X_a + 1) \times c_o(f(i,j) - X_a)$
    end if
  end for
end for

3.3.5 Homomorphic filtering

Homomorphic filtering is based on an image model, which considers the image to be a combination of reflectance and illumination.

$$f(x,y) = i(x,y)r(x,y) \tag{3.12}$$

The reflectance factor is mainly responsible for the contrast in the image, where as the illumination controls the dynamic range of the image. As the illumination is a low frequency component it can be filtered to achieve smooth contrast, by using a high pass filter.

To take the Fourier transform, *log* is taken to separate the individual components. Equation: 3.13 shows the separation of the components using *log*.

$$\begin{aligned} \log(f(x,y)) &= \log(i(x,y) \times r(x,y)) \\ f_l(x,y) &= i_l(x,y) + r_l(x,y) \end{aligned} \tag{3.13}$$

Then the Fourier transform of equation: 3.13 is taken as shown in equation: 3.14

$$\begin{aligned} \mathcal{F}(f_l(x,y)) &= \mathcal{F}(i_l(x,y) + r_l(x,y)) \\ F_l(u,v) &= I_l(u,v) + R_l(u,v) \end{aligned} \tag{3.14}$$

The high pass filter $B(u,v)$ used to filter the illumination effect is the Butterworth filter represented by equation: 3.15.

$$B(u,v) = \frac{1}{1 + (\sqrt{2}-1)(D_0/D(u,v)^{2n})} \tag{3.15}$$

where, $D(u,v) = (u^2+v^2)^{1/2}$, D_0 is the locus, n is the order of the filter.

The filter is applied on the Fourier transform of the image as shown in equation: 3.16

$$S(u,v) = B(u,v)(I_l(u,v) + R_l(u,v)) \tag{3.16}$$

The inverse Fourier transform (shown in equation: 3.17) followed by the exponent (shown in equation: 3.18) is taken to retrieve the original image.

$$s(x,y) = \mathcal{F}^{-\infty}(B(u,v)(I_l(u,v) + R_l(u,v))) \tag{3.17}$$

$$g(x,y) = \exp(s(x,y)) \tag{3.18}$$

4 Pipeline implementation

As discussed in the first chapter the objective of the thesis is to implement a radiometric enhancement pipeline which can be used on-board the robotic lander to enhance the performance of the BSM module. This chapter provides details on this pipeline and its implementation.

4.1 Pipeline structure

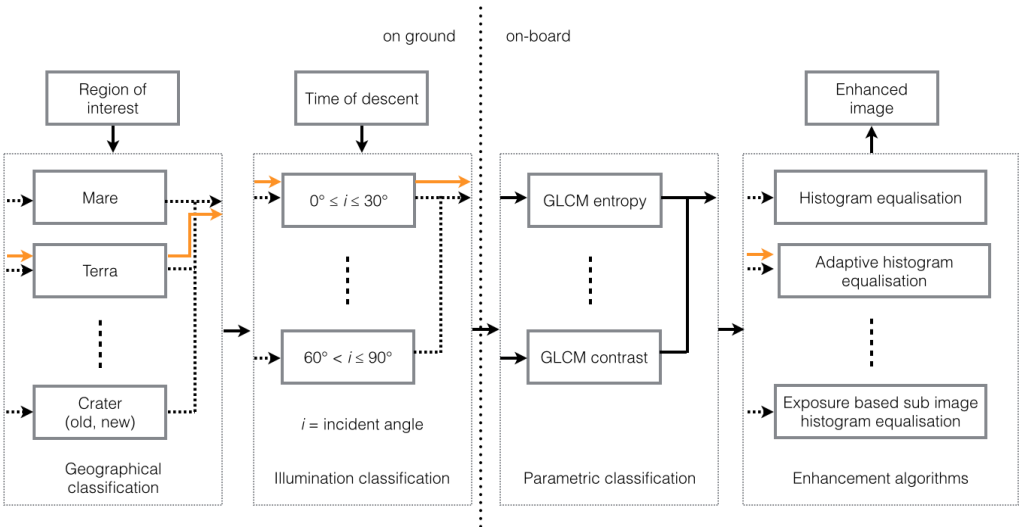

Figure 4.1: Overview of the radiometric enhancement pipeline structure

The overview of the radiometric enhancement pipeline structure is shown in figure: 4.1. The pipeline structure is divided into two main parts, in the first part the image is classified based on the classification of images discussed in chapter: 3, followed by the second part where the image is enhanced using the selected method. The image classification part starts with the geographical classification. This classification is done at the mission design centre as the landing site is known.

During the descent phase the first classification is based on the time of descent. The time of descent provides the position of the sun with respect to the Moon and hence the the incidence angle.

The next classification step is made based on the mathematical parameters computed from the real image data. These properties are computed based on the GLCM matrix values (such as contrast) as proposed in the second chapter. A classification logic is developed based on the classification parameters and the outcome of the logic is used to select the enhancement algorithm. Based on a combination of the values of individual parameters, an enhancement algorithm is selected. The classification logic is developed based on a training data set (explained in chapter: 5).

This classification is important as the images vary in grey level distribution, illumination condition, local contrast and global contrast and a single enhancement algorithm might not be sufficient for all kinds of images.

4.1.1 Geographical classification

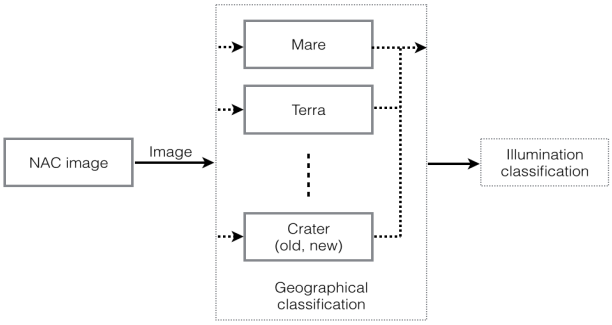

Figure 4.2: Image classification based on geographical information

The first stage of the pipeline is to classify the image based on geographical information as shown in figure: 4.2. Based on chapter: 2, the data set is classified into different images based on surface reflectance, topography and surface features based on the landing site. The first classification is based on surface reflectance. Again the surface of Moon has two dominant regions mare and terra. Mare regions are a relatively dark, whereas terra region is relatively old, bright highlands. Due to its old age, the crater content is much denser in terra region compared to mare region. Hence with respect to the BSM requirements, terra has the most suitable geography as more craters mean more shadows.

Figure: 4.1 also shows a possible path, shown in orange colour arrow taken by an image. To explain the pipeline, the image shown in figure: 4.3 is regarded as a desired landing site. Based on visual inspection it can be concluded that the image belongs to high reflectance terra region.

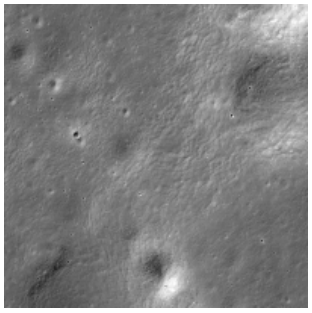

Figure 4.3: Image of a terra region with craters

The terrain of the Moon can be further classified based on its topography, namely

plains, mountains and rilles. The source of shadows in plains are the surface features like craters, boulders and fractures. Some regions are a combination of a flat region and mountains, or a flat region and rilles. Generally, mountains are large features and hence depending on the incidence angle are a source of large shadows. Rilles are grooves in the surface of the Moon,they are a source of structured shadows and could act as strong markers for pose estimation. The image shown in figure: 4.3 contains old craters, has no mountain or any other topographical feature.

4.1.2 Illumination classification

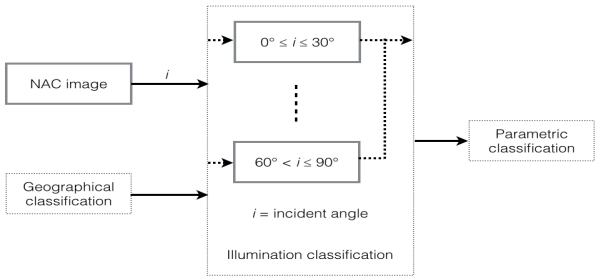

Figure 4.4: Image classification based on illumination angle

As shown in figure: 4.4, during the descent phase, the image is classified based on the incidence angle, which depends on the time of descent. The incidence angle combined with Lunar surface features are responsible for the size and strength of the shadows. As the Moon has virtually no atmosphere, the shadows are classified as hard shadows. The factors affecting the strength of the shadows are the incidence angle and the surface reflectance. At low incidence angles the intensity of the light is high and the reflected light from the surface reduces the strength of the shadows.

For incidence angles, i.e. sun is high on the Lunar horizon between 0^o and 20^o the amount of shadows observed in the images are negligible and hence the use of BSM based navigation at these angles is not possible. At high incidence angles (values between 60^o and 80^o) the shadows are hard and distinct from the surface and are highly suitable for BSM to be used for matching and pose estimation.

Figures: 4.5 to 4.7 show the effect of illumination at different incident angles. As it can be observed, it is difficult to differentiate between the shadow and the surface in figure: 4.5 at a low incidence angle in a mare region. Whereas with an increase in incidence angle, the distinction between the surface and the shadows becomes more prominent.

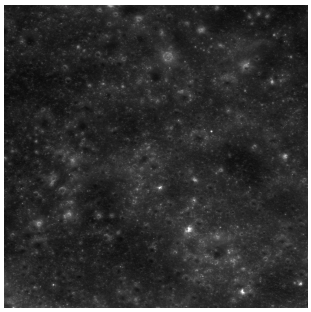

Figure 4.5: Illumination with incidence angle $i = 15.02^o$

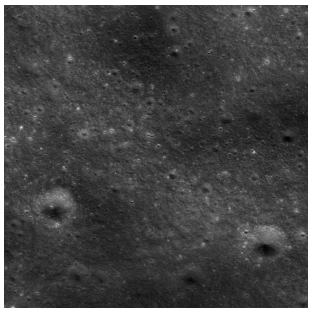

Figure 4.6: Illumination with incidence angle $i = 45.0^o$

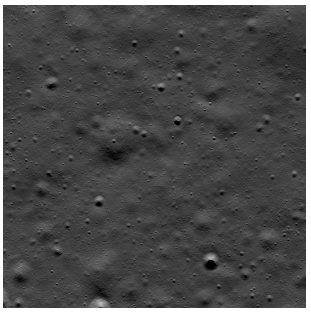

Figure 4.7: Illumination with incidence angle $i = 75.1^o$

4.1.3 Parametric classification

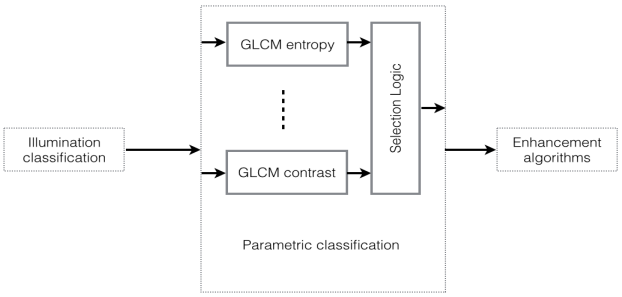

Figure 4.8: Parametric classification

This section of the pipeline implements the logic to select the enhancement algorithm, based on the outcome of the image classification logic as shown in figure: 4.8. The classification logic is a combination of four parameters namely GLCM correlation, GLCM contrast, GLCM entropy and Image entropy as explained in chapter: 2. The GLCM correlation provides the linear dependency of a grey value with its neighbour and hence it provides the level of the measure of smoothness in the image, GLCM contrast provides the contrast level of the image and GLCM entropy provides the measure of the contrast distribution in the image. Image entropy gives the randomness of the grey values in the image. As these four parameters cover the possible variations in a grey scale image, a classification based on these parameters is expected to be robust.

Table: 4.1 shows different parameter values of two images. The images selected are of two different regions, figure: 4.9 is from a mare region, whereas the image in figure: 4.10 is from a terra region. As it can be seen, the values of the parameters depend on the image contrast, and hence they can be used as classifier.

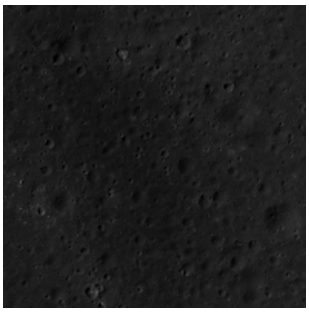

Figure 4.9: Image of a mare region

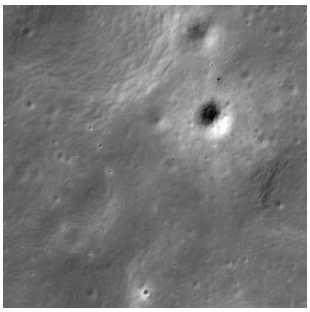

Figure 4.10: Image of a terra region

Parameter	Figure: 4.9	Figure: 4.10
GLCM correlation	0.423379	0.830038
GLCM contrast	44.5753	1814.31
GLCM entropy	6.02499	7.06847
Image entropy	4.07680702209	5.67372512817

Table 4.1: Values of different classification parameters

4.1.4 Enhancement algorithms

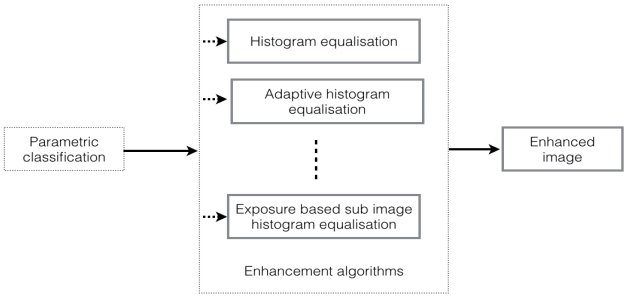

Figure 4.11: Enhancement algorithm

In this section all the selected enhancement algorithms as shown in figure: 4.11 (explained in chapter: 3) are implemented. After the selection of the enhancement algorithm by the parametric classification logic, the image is enhanced using the selected method. Histogram equalisation is expected to work well on images with low GLCM contrast values. AHE and CLAHE are expected to work well on images with high contrast value, while CLAHE should limit the saturation effect in the images. ESIHE is expected to work well on the low exposure images and Homomorphic filtering (by using a high pass filter) should filter the low frequency illumination in the image.

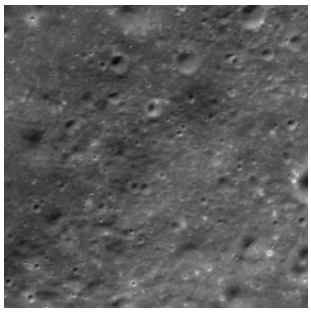

Figure 4.12: Original NAC image

Figure 4.13: HE enhanced image

Figure 4.14: AHE enhanced image

Figure 4.15: CLAHE enhanced image

Figure 4.16: ESIHE enhanced image

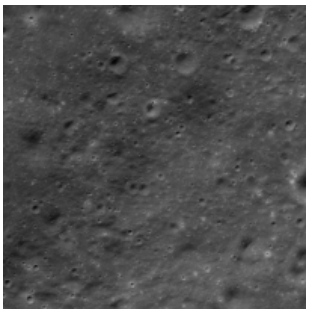

Figure 4.17: HF enhanced image

Figures: 4.12 to 4.17 (NAC image M1162384686RC) show the original image and in sequence the HE, AHE, CLAHE, ESIHE and HF enhanced images. As it can be seen, the HE and the AHE methods gives a more binary appearance, whereas CLAHE and ESIHE give a smooth appearance by clipping the histogram. Whereas, homomorphic filtering reduces the illumination effect in the image.

5 Experiments

The purpose of the radiometric enhancement pipeline is to enhance the capability of the BSM system by reducing the effects of uneven illumination and surface texture on the shadow segmentation. The implemented pipeline shall provide an equalized output, irrespective of the surface texture, for a specified range of incidence angles. It should be able to suppress the brighter regions (new craters, sharp peaks) in the image and create a contrast between the dark regions and shadows to avoid false shadow identification.

To validate the implemented pipeline, NAC images from the LROC camera are used instead of real descent images, as they are the most complete data source. The virtual images rendered from the corresponding DTM file of NAC images are used as reference images. The performance of the enhancement method is tested by comparing the shadow information of the enhanced image with the shadow information of the rendered image, as this affects the performance of the BSM.

This chapter describes the experimental set-up used in the thesis. The chapter starts with a description of the instrument overview of LROC and then explains the different image formats available from the LROC and which are used as input data. The next section explains the methods used to validate the pipeline.

5.1 Image source

The images taken by the LROC[1] will be used as experimental data. Among the various available databases of Lunar images from recent missions such as LROC, SELENE, Chandrayan, etc., LROC was selected because of the following reasons:

1. Large amount of (2D) images available with meta-data[2]: The database of the LROC provides images of the whole Moon and for some locations the images are available for different incidence angles.

2. High resolution of images: As the BSM is proposed to be used at a lower altitude, the surface detail captured by the on-board camera will be higher than the surface detail provided by the camera in a Lunar orbit. Therefore, it is important to select the Lunar images with the highest available resolution, in order to simulate descent image conditions. A review of available Lunar images suggested that the data taken from the NAC camera during the LRO mission are of high resolution of up tp 0.5 *m/pixel*, hence they were selected to validate the performance of the pipeline.

[1]LROC is an instrument of LRO satellite launched for exploration of Moon[27]

[2]The meta-data of the image provides a description of the image. The information contained by the meta-data includes details of the instruments, spacecraft, incidence angle, image content and geographical region covered in terms of latitude and longitude among others

3. DTMs available for rendering: Even though LROC was not designed for stereo image generation, DTM files are generated by slewing the spacecraft. Large data set of DTMs corresponding to high resolution images are available for rendering and analysis purposes.

5.2 LROC instrument overview

The instruments were studied to understand the resolution and information content of the images in more detail, as the various available image formats depends on the camera type and their resolution. Further more it is important to understand the sensors as they image and its content.

LROC consists of three major components:

1. Narrow angle camera
2. Wide angle camera
3. Sequencing and compressor system

5.2.1 Narrow angle camera

LROC has two NACs, each with 700 *mm* focal length, a 5064 pixel line array Charge Couple Device (CCD) and a cross-track field of view of 2.8502^o for the left camera and 2.8412^o for the right camera. Each pixel value is sampled with a 12 *bit* Digital to Analog Converter (DAC) which is then companded to 8 *bit* before being stored into the internal NAC buffer of 256 *MB*. This gives a full resolution image dimension of $52,224 \times 5064$ *pixels*. The NAC is designed to have a spatial resolution of 0.5 *m/pixel*, though it varies with the altitude of the LRO satellite. The information is taken from LROC manual [2].

5.2.2 Wide angle camera

LROC is equipped with one Wide Angle Camera (WAC), with a 1024×1024 pixel area array CCD. WAC captures images in different wavelengths (visible, near infrared and ultraviolet). Each pixel value is sampled with a 11 *bit* DAC which is then companded to 8 *bit*. The WAC is designed to have a spatial resolution of 100 *m/pixel*, though it varies with the altitude of the LRO satellite [2].

5.2.3 Sequencing and compressor system

LROC is equipped with one Sequencing and Compressor System (SCS), which is responsible for the sequencing of the image acquisition by NAC and WAC. SCS performs a lossless compression of the images before storing it to the spacecraft data system [2].

5.3 Image formats and image processing

The images acquired by NAC are available in three formats, Experiment Data Record (EDR),Calibrated Data Record (CDR) and Pyramid Tagged Image File Format (PTIF) [2]. Raw images from NAC are stored as a sequence of even and odd pixels, divided with 1 *MB* of padding data. Every 1 *MB* of data is followed by a 20 *byte* context camera heritage header. At Science Operation Center (SOC) the even and the odd pixel data is extracted and interleaved together to obtain the actual image. Further data from the meta-file and the SOC database are combined together to form the Planetary Data System (PDS) label of the EDR file. Each (from left and right NACs) EDR image is stored in 8 *bit* format with a maximum image dimension of $52,224 \times 5064$ *pixels*. Based on the number of lines requested (programmed by the user) for each image the size of the EDR images may vary (it would always be less than or equal to the specified dimension of $52,224 \times 5064$ *pixels*, as the memory of 256 *MB* is fixed) [2].

Each image from left and right NACs is radiometrically calibrated to radiance or I/F (reflectance). The radiance images are calibrated to 4 *byte* floating value. I/F images are converted to 2 *byte* signed integer values [2]. The CDR images are processed at SOC on ground, the calibration method is explained in [35]. PTIF images are compressed multi resolution images obtained from CDR images [2].

5.3.1 Image type for pipeline validation

The CDR files are created after the calibration of EDR files at SOC for non-linearity, sensitivity, spectral response, dark noise and geometric alignment [35]. The calibration process improves the raw image and brings out more information.

Due to their high image quality CDR images were considered over EDR images for the validation of the pipeline. Although CDR images of LROC are calibrated at SOC, it is assumed that at least a basic form of the calibration of the raw images in a real mission will be done on-board the spacecraft.

The list of selected DTM files used for virtual image rendering and their corresponding NAC images are provided in appendix: A.

5.4 Virtual image rendering

The DTM files for virtual image rendering were taken from the LROC website [47]. The DTM files are generated using two NAC pairs (left and right) combined with the Lunar Orbiter Laser Altimeter (LOLA) data. To generate the DTMs, a combination of two software are used. The Integrated Software for Imagers and Spectrometers (ISIS) from the United States Geological Survey (USGS) and SOCET SET from BAE systems. The DTM file generation technique is discussed in detail by Tran et al. [4].

The fact that the DTM files are generated using the NAC images is advantageous for this thesis. The virtual images rendered from the DTM files are used as the reference images and the corresponding NAC images are used instead of descent images.

5.4.1 Virtual image rendering process

The virtual image rendering method was provided by the German Aerospace Centre. As shown in figure: 5.1, from the Geospatial Tagged Image File Format (GeoTIFF) (DTM file) the latitude, longitude and height information is extracted using the method described by Bowman-Cisneros and Eliason in [3] [appendix: B]. The transformation to Cartesian coordinates is done using the equations provided by the National Oceanic and Atmospheric Administration (NOAA) [30].

With the help of SPICE kernels[1] where the NAC was while taking a certain image is calculated in the Lunar coordinate system. SPICE is also used to obtain the illumination condition using the solar ephemeris.

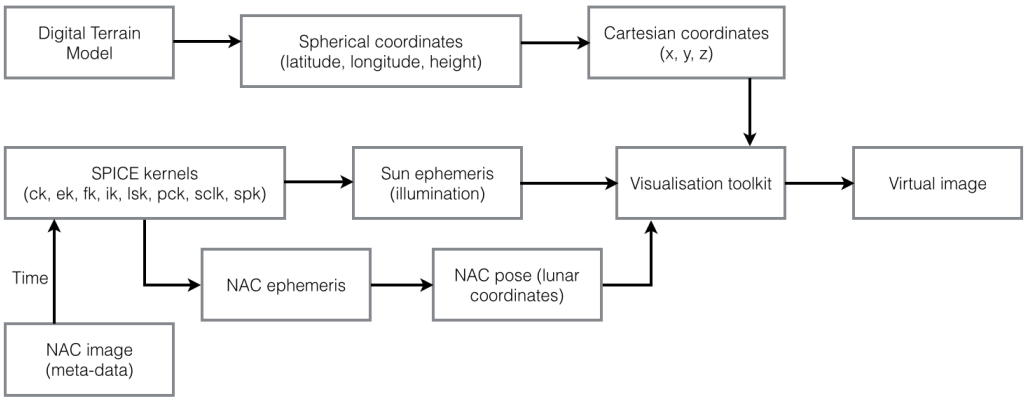

Figure 5.1: Virtual image rendering process

Rendering Resolution

The resolution of DTM files varies based on the resolution of the NAC images. The resolution of the NAC images in turn depends on the altitude of the LRO. The selected DTM files have two spatial resolutions 2 *m/pixel* and 5 *m/pixel*. Further due to memory limitations during the full scale rendering of the virtual image, the resolution of the DTM was reduced by a factor of 4. The NAC images were accordingly binned to compensate for the resolution loss in the rendered image. The binning factor for NAC images is computed as:

$$b_f = \frac{r_D.S_f}{r_N} \tag{5.1}$$

[1]the SPICE kernel contains navigation and other ancillary information of spacecraft, spacecraft instruments and some celestial bodies, refer [29] for more information on SPICE kernel types and their content

where, r_D is the spatial resolution of the DTM in *m/pixel*, S_f is the scale factor with which the resolution of the DTM is reduced, r_N is the resolution of the NAC image in *m/pixel* and b_f is the binning factor. The new width and height of the NAC image is calculated as:

$$w_n = \frac{w_o}{b_f} \tag{5.2}$$

$$h_n = \frac{h_o}{b_f} \tag{5.3}$$

where, w_o and h_o are respectively the width and the height of the NAC image, w_n and h_n are respectively the width and the height of the binned image.

The images from DTM files are rendered using the width and height calculated from equations: 5.2 and 5.3. The rendering resolution of all the selected DTM files and the corresponding NAC images is listed in appendix: C.

5.4.2 Correction of shift between NAC images and rendered images

The virtual images rendered using the method explained in section: 5.4 differed from the NAC image in spatial feature location. There was shift in North-South and/or East-West direction. A further investigation revealed that the DTM files are not ground locked, i.e. there could be deviation in the latitude, longitude and height and hence the spatial discrepancy in rendered image is justified. The spatial shift was manually fixed by using the pitch angle to fix the East-West shift and further use a manual comparison to fine tune the accuracy.

Initially and based on the assumption of ground locked DTMs and NAC images, the validation of the implemented pipeline was based on an automated test between the segmented shadows of rendered image and segmented shadows from enhanced image on a very large database of approximately 500 DTMs. Due to the now necessary manual pre-processing involved, it was decided to use only 20 DTMs and split them up in tiles in order to achieve a database large enough for testing.

Pitch offset calibration

As mentioned earlier the rendered images were not at the same position as the NAC images, as there was always an offset towards left-right or/and up-down direction. On analysis, it was observed that the offset in left-right direction is high (up-down offset was low and it has been taken care of manually) and hence to fix this a pitch angle was added in the rendering process. The value of the pitch angle was selected after multiple iterations based on manual comparison of the NAC images and the rendered images.

Manual offset calibration

In order to improve the spatial match between the NAC image and the rendered image an offset was set during the cropping. The offset value was calculated by selecting four features in a NAC image and find the pixel location of the features in the rendered

image. Let's consider that the four selected features are $F1$, $F2$, $F3$ and $F4$ and their corresponding locations in NAC image are $(X1_N, Y1_N)$, $(X2_N, Y2_N)$, $(X3_N, Y3_N)$ and $(X4_N, Y4_N)$ respectively and their corresponding locations in rendered image are $(X1_V, Y1_V)$, $(X2_V, Y2_V)$, $(X3_V, Y3_V)$ and $(X4_V, Y4_V)$. Using these points the offset for column o_x is calculated using equation: 5.4 and the offset for row o_y is calculated using equation: 5.5.

$$o_x = \frac{X1_N - X1_V + X2_N - X2_V + X3_N - X3_V + X4_N - X4_V}{4} \tag{5.4}$$

$$o_y = \frac{Y1_N - Y1_V + Y2_N - Y2_V + Y3_N - Y3_V + Y4_N - Y4_V}{4} \tag{5.5}$$

These offset values were used during the cropping of the NAC image in order to match the spatial feature location. With this method the offset in spatial feature location was reduced to less than 3% for most of the cases. The offset percentage was obtained by selecting four spatial features in the cropped NAC image and comparing them with the same spatial features in the rendered image.

Additional issues

Even after the manual calibration, in some cases the deviation of the spatial feature match was higher than 5%. The offset percentage was obtained by selecting four spatial features in the cropped NAC image and comparing them with the same spatial features in the rendered image. On analysis, it was observed that in some cases the DTM rendered images were compressed at some locations and in some cases there was a variable angular shift in the top and at the bottom part of the rendered image.

The 20 calibrated DTM files were each divided in to 5 sub images making the total number of 100 images in the data set.

5.5 Experiment description

Based on the objectives from chapter: 1, the experiment was divided into two parts:

1. Performance analysis of selected enhancement methods
2. Performance analysis of the parametric classifier

5.5.1 Performance analysis of selected enhancement methods

To check for the first objective of the thesis, i.e. a suitable enhancement method with respect to shadow segmentation, the NAC images are enhanced using the selected enhancement methods and the performance of the enhancement methods is assessed using the shadow information. The shadow information from the enhanced image will then be compared with the shadow information from the rendered image. The

performance of each enhancement method is evaluated based on two factors. The first factor is the number of correct matches, i.e. the number of shadow points matched between the shadow segmented rendered image and the shadow segmented enhanced image, this is termed as the Matched Shadow Count (MSC). For example, consider that the total number of identified shadow from a image is 20 and the total number of identified shadows from an enhanced image is 23. Out of this, if 14 shadows match between the shadow segmented rendered image and the enhanced image, the MSC count is 14.

The second factor is the number of shadow points detected from the enhanced image which has no corresponding shadow in the rendered image, this is termed as the Unmatched Shadow Count (USC). Considering the previous example, the total shadow count from the enhanced image is 23 and the MSC value is 14. Hence, the USC value is $23 - 14 = 9$.

The analysis of MSC and USC tells the performance of an enhancement method. A value of MSC close to the shadow count from the rendered image, would mean that the performance of the enhancement method is good, where as a high USC value could mean two things. Either there are additional shadows from the enhanced image, which were not present in the rendered image or due to the enhancement some non-shadow regions are being identified as shadows. The first situation is only possible in real missions, where new craters are formed after the reference image was created. As the NAC images used are the same NAC images used to create the DTM file, this situation is not valid and hence all the USC values will be considered as noise.

Enhancement methods analysis

To perform the comparison, first the NAC image is resized based on the binning factor b_f as explained earlier. Then the images are enhanced, using the selected methods, followed by the shadow segmentation. The images from DTM files are rendered with the resolution w_n and h_n from the DTM file, followed by shadow segmentation as shown in figure: 5.2. The comparison is based on the location of shadow contour centroids on the image, in terms of row and column. Each centroid point from the rendered image is matched with the centroid points from the enhanced image, with a threshold. As mentioned earlier, even after manual calibration, there is a shift in the spatial feature location hence, a threshold value of 9 is selected.

Homomorphic filtering before enhancement

Another approach used is to apply HF before the enhancement as shown in figure: 5.2. As the homomorphic filtering removes the illumination effect, it is expected to reduce the effect of locally bright regions in the enhanced image and hence, provides a smooth contrast enhancement. For comparison of performance the MSC and USC values are compared with and without homomorphic filtering.

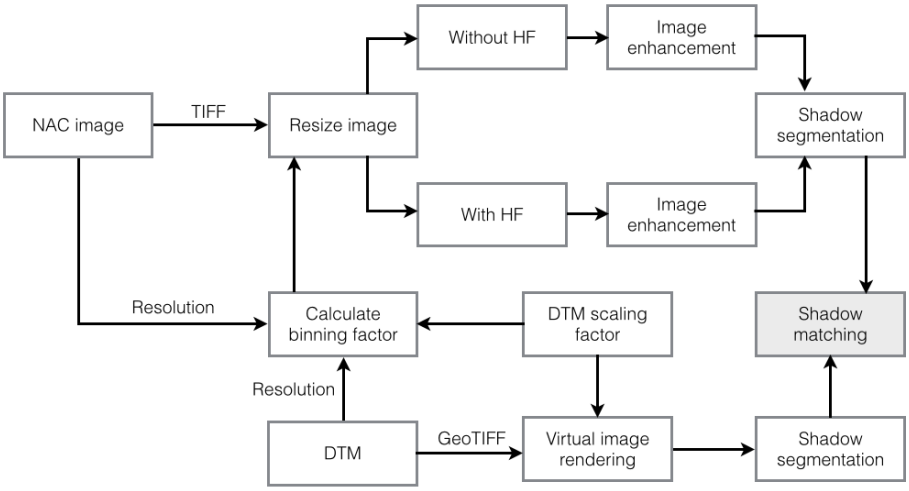

Figure 5.2: Experiment set-up to verify the enhancement pipeline

5.5.2 Performance analysis of the parametric classifier

The second objective of the thesis is to design an automatic classifier, based on the values of the parameters listed in chapter: 3. The first step is to find the values of the classifier based on the training data. The second step is to use the classifier values to select the suitable enhancement algorithms. Figure: 5.3 shows the structure of the training process.

Training process

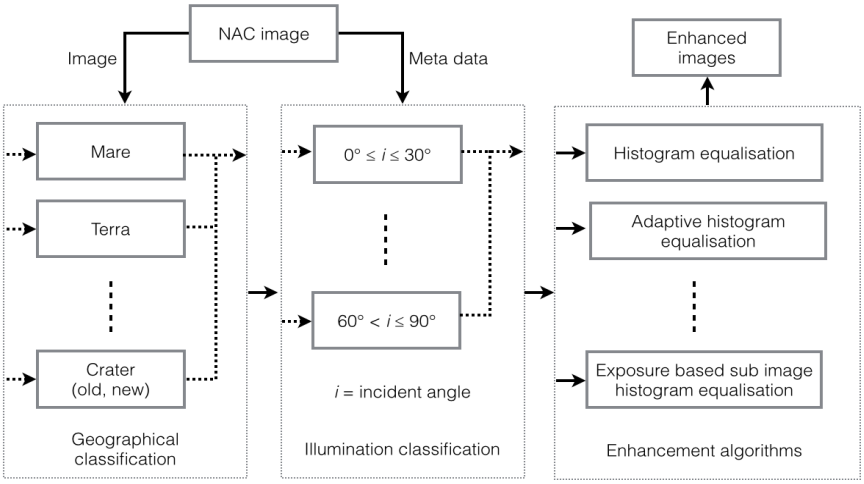

Figure 5.3: Training process for parametric classification

For training, 25% of the selected rendered images and there corresponding enhanced NAC images were used. During the training process GLCM entropy, GLCM contrast,

GLCM correlation and Image Entropy values were calculated for each image. The training data set of NAC images were enhanced using all the implemented algorithms and then the binary shadow image was generated. Each binary shadow image was compared with the corresponding binary shadow image of the rendered image and the best enhancement algorithm was selected based on the number of MSC. A relationship was established between the parametric values and the most suitable enhancement algorithm and this relationship was used to classify the images autonomously during the validation process, with a test data set.

Two methods were used to design the classification logic, in the first method the classifiers were given a weight based on the confidence. The confidence of the parameter was based on the standard deviation of that parameter, i.e. the lower the standard deviation, the higher the confidence.

Multiple linear regression was used as second option, where the parameter values were used as independent variables and the enhancement methods were used as dependent variables. Each enhancement method was allocated a number and treated as an output of the model.

Validation process

The implemented pipeline as shown in figure: 4.1 is used during the validation process with the remaining 75% images. During the validation process the automatic classification logic developed during the training process is used. The validation process is classified into two steps.

Step 1

In the first step, by using the classification logic developed during the training phase the images in the test data set are enhanced and the corresponding binary shadow images are generated, which are then compared with the corresponding binary shadow images of the rendered images.

Step 2

The second step is to verify the performance of the autonomous classification method. The idea behind this step is to ensure that the selected enhancement method by the classification logic is valid and selects the correct enhancement method for all test images. The test image set is executed on all the enhancement algorithms and for each of them, binary shadow image is generated, which is compared with the corresponding binary shadow image of the rendered image. The MSC value from the classifier selected algorithm is compared with the MSC values from all the selected methods. If the MSC value for the selected algorithm is the highest, then the classifier selection is correct.

5.6 Expected results

This section discusses the expected results from the experiments. As the idea is to identify the correct shadows using the enhancement algorithms, first the expected

results from different algorithms are explained, followed by the expected results for classifier performance.

5.6.1 Enhancement methods

The expected performance of each of the enhancement methods is listed below:

1. Histogram equalisation: HE shall work well on images with low dynamic range (low contrast). In cases where both the foreground and the background are either bright or dark the HE is expected to perform well.

2. Adaptive histogram equalisation: As the AHE uses the local histogram to enhance the image, the AHE shall perform well with images with local brightness.

3. Contrast limited histogram equalisation: The principal of the CLAHE is to limit the contrast level and hence avoid the saturation effect. The CLAHE images shall provide less noise amplification.

4. Exposure based sub-image histogram equalisation: ESIHE method should be able to enhance the contrast of low exposure images.

5. Homomorphic filtering: Homomorphic filtering shall remove the uneven illumination effects and keep the reflectance of the surface.

5.6.2 Parametric classifier

The performance of the classifier is evaluated based on the ability of the classifier to select the correct enhancement method, based on the values of different parameters. An acceptable classifier must exceed 90% of correct selections of the best enhancement methods.

6 Results and discussion

This chapter discusses the results obtained in the thesis. The chapter is divided into two parts based on the experimental set-up explained in the previous chapter. The first part shows the result of different enhancement methods in terms of shadow segmentation and compares them with the performance of the original image. The performance of the enhancement methods based on geographical features and incidence angle is discussed in the next part. Followed by the performance of the parametric classifier.

6.1 Performance of selected enhancement methods

As the goal is to evaluate the performance of the enhancement methods using the shadow information, the first step was to identify the rendered and NAC images with shadow content.

Shadow information analysis

Out of 100 selected rendered and NAC image pairs, that were chosen for the experiment, only 74 of the rendered images (RI) contained shadows, as shown in figure: 6.1.

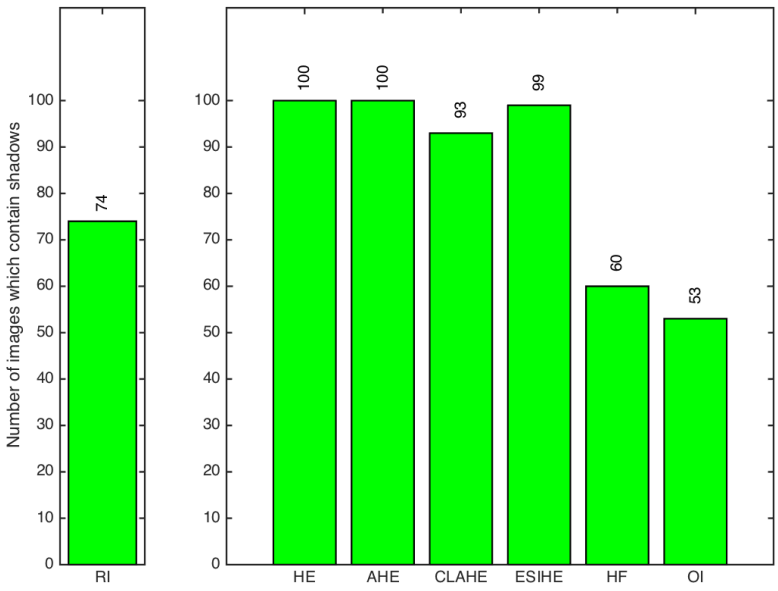

Figure 6.1: The number of images which contain shadows, for the rendered images (RI), each of the enhancement method and the original images (OI)

It is also evident from the figure: 6.1, that all the HE and the AHE enhanced images contain shadows. Since the total number of rendered images with shadow content

is 74, 26 images that were enhanced using the HE and the AHE method contain false shadows. Whereas, out of 100 images enhanced using CLAHE and ESIHE, 7 and 1 images, respectively, contain no shadows. As can be seen in figure: 6.1, the performance of the HF and shadow segmentation using the Original Images (OI) is worst with 40 and 47 images, respectively, without shadows.

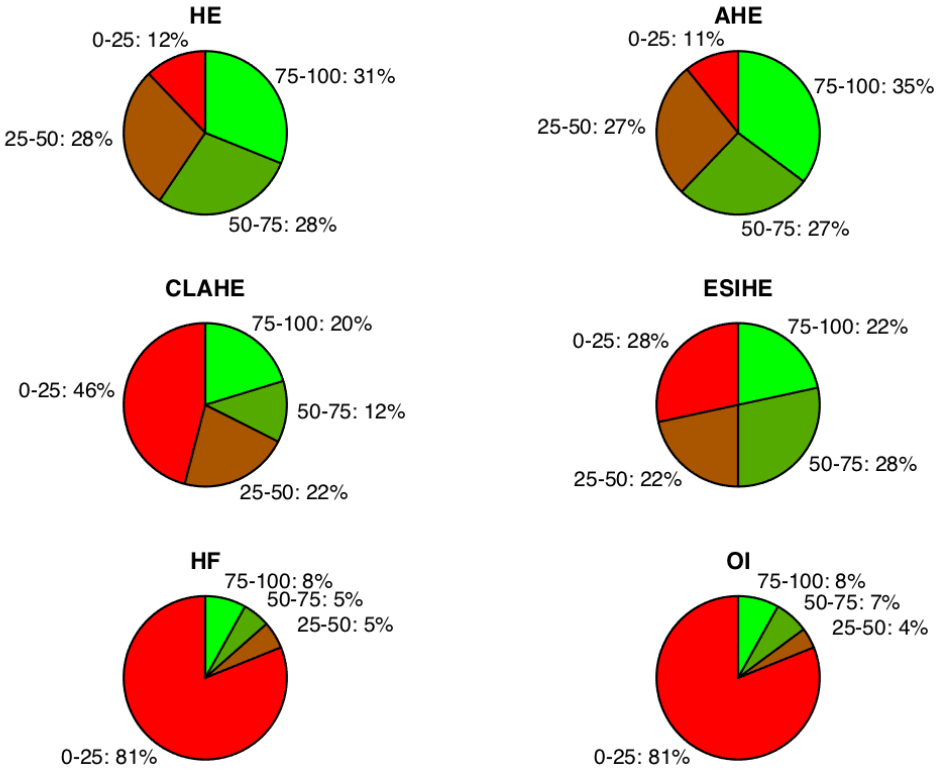

Figure 6.2: The pi-charts show the distribution of images in terms of $\%MSC$ in four regions: $0-25$, $25-50$, $50-75$ and $75-100$

The pi-charts in figure: 6.2 show the performance of each enhancement method in terms of $\%MSC$. The $\%MSC$ is calculated using the equation: 6.1.

$$\%MSC = \frac{MSC}{N_{vi}}100 \tag{6.1}$$

where, N_{vi} is the total number of shadows detected in the rendered image and MSC is the number of matched shadows between the rendered and the NAC image, as explained in the previous chapter.

Based on the $\%MSC$ images were distributed into four categories $0-25$, $25-50$, $50-75$ and $75-100$ for each enhancement method. To make this more clear, 16 images enhanced by using the CLAHE method has $\%MSC$ between $25-50$. Hence,

as shown in figure: 6.2, for range $25 - 50$ the percentage is $(16/74) \times 100 \simeq 22$. As is visible in the figure: 6.2, the AHE has highest percentage of MSC between $75 - 100$, followed by the HE. The CLAHE and the ESIHE has approximately the same performance. The performance of the HF and the OI is worst, as 81% of the images have $\%MSC$ between $0 - 25$.

From the above result, it is evident that the image enhancement is necessary before shadow segmentation to detect more number of correct shadows. From figure: 6.1, it can be concluded that for shadow detection, image enhancement is necessary as no shadows were detected in 21 original images. Figure: 6.2 shows that the number of matched shadows between the rendered image and the NAC image also increases after enhancement. The percentage of images with $\%MSC$ between $0 - 25$ is 81% for original image, whereas for the AHE, it is 11%.

The performance of the HF and the OI are not considered to be satisfactory, hence they are not used for further comparison. As only 74 rendered images contain shadows, only these rendered and NAC image pairs were used to evaluate the enhancement methods.

MSC and USC analysis

As explained in the previous chapter, MSC is the count of the number of shadows matched between the rendered image and the real image. If an enhancement method would lead to segmentation of all the shadows which are present in the rendered image, the $\%MSC$ would be 100. Hence higher the $\%MSC$, better the enhancement method. A categorical distribution of $\%MSC$ for all the enhancement methods is shown in figure: 6.2. The percentage of images with the $\%MSC$ between $75 - 100$, is the highest for the AHE (35%), followed by the HE (31%), the ESIHE (22%) and the CLAHE (20%) as depicted in figure: 6.2. The performance of the enhancement algorithms are similar for the other $\%MSC$ ranges ($50 - 75$, $25 - 50$, $0 - 25$).

Another important aspect identified by Kaufmann et al. [18] in BSM is the USC, the shadow points identified in descent image which do not match with the shadow points in the reference image. These points have a negative low weight in the BSM, which reduces the overall match percentage between the reference and the descent image. Even though the weight allocated to a USC point is low compared to a MSC point, higher number of USC points can affect the matching process. Hence, the analysis of USC points in the shadow segmented enhanced image is important. The $\%USC$ is calculated as per equation: 6.2.

$$\%USC = \frac{TSC - MSC}{TSC} 100 \tag{6.2}$$

where, TSC is the total shadow count from the enhanced image.

The number of USC points for all the algorithms are higher than the number of MSC points. As shown in figure: 6.3 the distribution of USC for HE and AHE enhanced images are more concentrated towards higher percentage. Whereas, the distribution of USC is relatively more sparse for CLAHE and ESIHE, hence per MSC the number of USC is less.

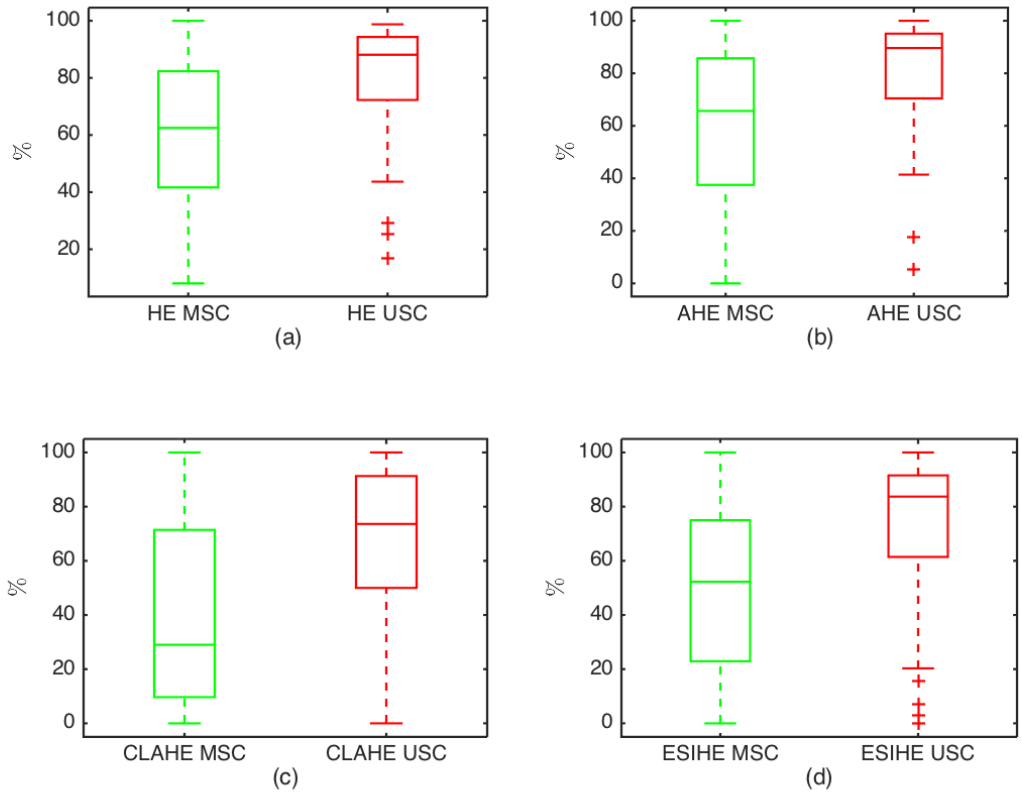

Figure 6.3: Comparison of $\%MSC$ and $\%USC$ for the selected enhancement methods

To get an absolute difference between the shadow segmented enhanced image and the shadow segmented rendered image an XOR operation is used. XOR is a simple and efficient operation to check the similarity between the shadow segmented images. If the two images are identical the summation of XOR value should be zero. The XOR values increases with increase in the dissimilarity between the two images.

Figure: 6.4 shows the distribution of the normalised XOR values of the enhanced images. The XOR value is normalised by dividing the total number of 1 in the XOR result with the total number of pixels in the image.

As shown in figure: 6.4, AHE enhanced images have the highest XOR value meaning it differs more from shadow segmented rendered images compared to other methods. CLAHE has the least difference, as the distribution is aligned towards 0. The XOR box plot is the normalised plot with summation of XOR value divided by the total number of pixel in the image.

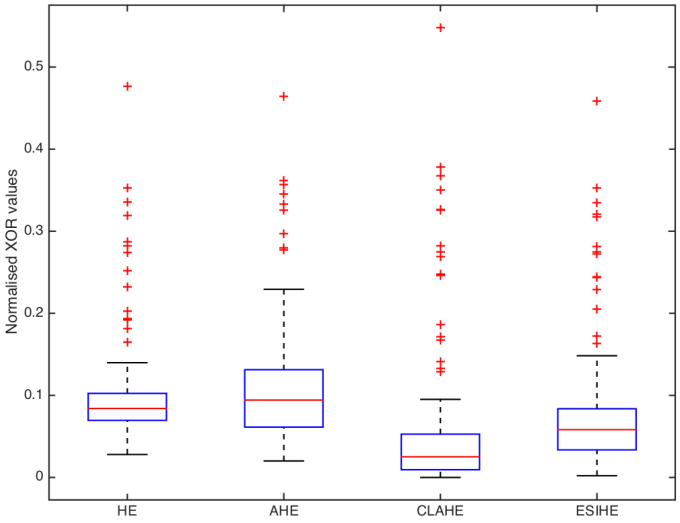

Figure 6.4: Normalised XOR values of the images for each enhancement method

The analysis of the MSC and USC plots shows that, the enhancement algorithms with high MSC also has the drawback of high USC value. This means that, due to enhancement, surface regions of the image also being classified as shadows. The enhancement stretches the dynamic range of the image and relatively darker surface regions due to thresholding are wrongly classified as shadows. Further analysis of this failure reviles that, the shadows in the selected NAC images are not hard in terms of visual interpretation. This is due to the low incidence angle, as the DTM files are created only using NAC images at low incidence angle due to information requirement.

Applying HF before enhancement

Another method investigated was to preprocess the original images, before applying the enhancement method. This was implemented with an objective to remove the illumination effect from the images before enhancing them. The illumination effect causes unwanted local brightness in the images and this affects the enhancement of the images. The performance of the enhancement with and without HF preprocessing was compared with respect to MSC and USC percentage.

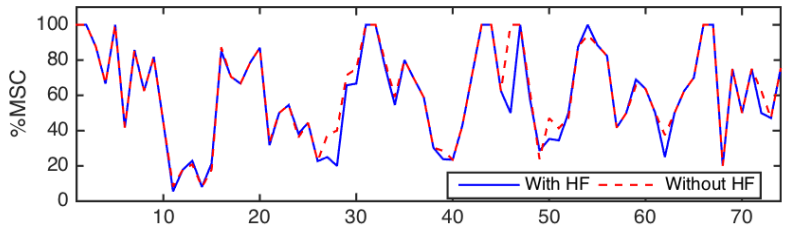

Figure 6.5: MSC comparison of preprocessed image for HE

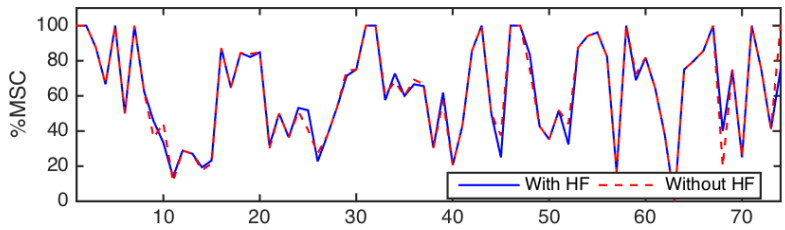

Figure 6.6: MSC comparison of preprocessed image for AHE

As shown in figure: 6.5 and 6.6 the percentage of the total number of detected MSC points remains same, except one or two cases where it increases by a small margin, but in most of the cases it is below the percentage of MSC without preprocessing. As shown in figure: 6.7 and 6.8 the percentage of the total number of detected USC points remains almost same with slight variation.

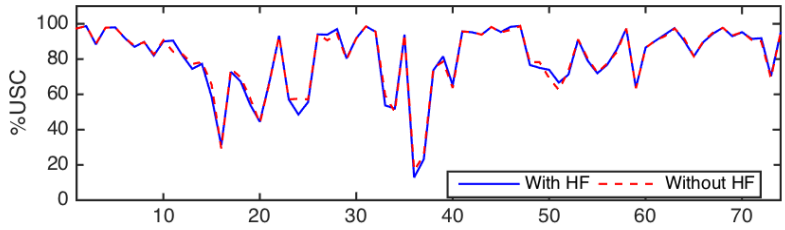

Figure 6.7: USC comparison of preprocessed image for HE

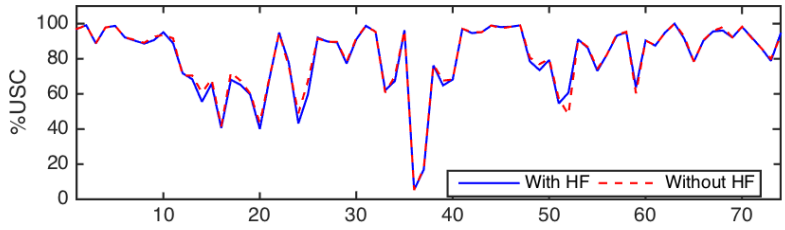

Figure 6.8: USC comparison of preprocessed image for AHE

Hence, the HF pre-processing does not seem to have an effect on the number of MSC points or on the number of USC points. This may be because reducing the illuminance, affects all the pixels and the dynamic range of the image remains close to the dynamic range value without HF filtering.

6.2 Automatic image classification

This section discusses the shadow segmentation performance of enhanced images with respect to the classification techniques discussed in chapter: 2. First the performance of the enhancement methods is compared with respect to the geographical information,

then a relation between the incidence angle and the enhancement methods is presented. Later the performance of the automatic classifier is discussed.

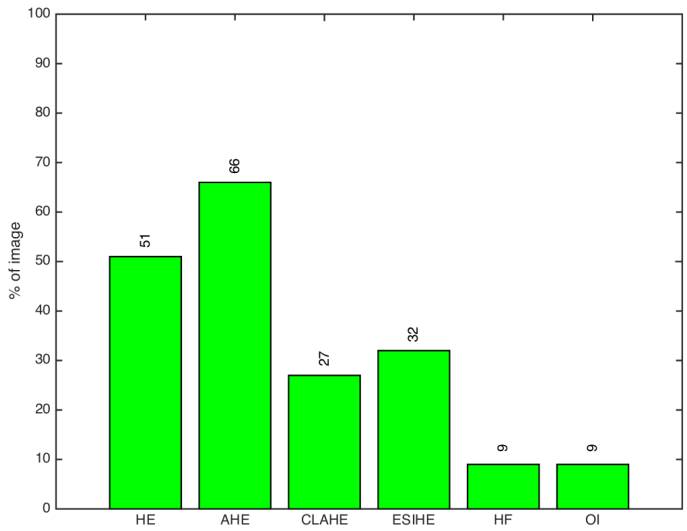

Figure 6.9: Percentage of images, for each enhancement method with the highest MSC value

Figure: 6.9 shows the percentage of images for which the performance of the enhancement method was best. As can be seen from the figure, there is no unique method which is applicable on all of the images. Hence, a pipeline based on automatic classification of images is required.

For some of the images multiple enhancement techniques show the same number of maximum MSC points. Out of 74 images, only 46 images had a unique enhancement method. Therefore, only these images were used to train and test the classifier logic. It is to be noted that, none of the images had HF as the unique best performer and so was the case with original image, hence they are not considered in the classification analysis.

Surface reflectance and incidence angle comparison with the enhancement methods

A detailed list of the selected DTMs and the region type they cover is mentioned in appendix: D. The analysis of the shadow segmentation results showed that the selection of image enhancement was largely dependent on the surface reflectance. As shown in figure: 6.10, the performance of HE and AHE are dominating in all the regions. In low reflectance region approximately 5% of the images worked well with CLAHE and 10% with ESIHE, but the majority of the images enhanced using HE and AHE showed better performance. This is also true for high reflectance region, the overall dynamic range of the image in high reflectance region is low and hence HE and AHE are the best applicable methods.

For the region with a combination of low and high surface reflectance the performance

of CLAHE and ESIHE increases to 15% and 20% respectively, even though HE and AHE are dominant, the result supports the argument that for high dynamic range images the performance of CLAHE and ESIHE is better.

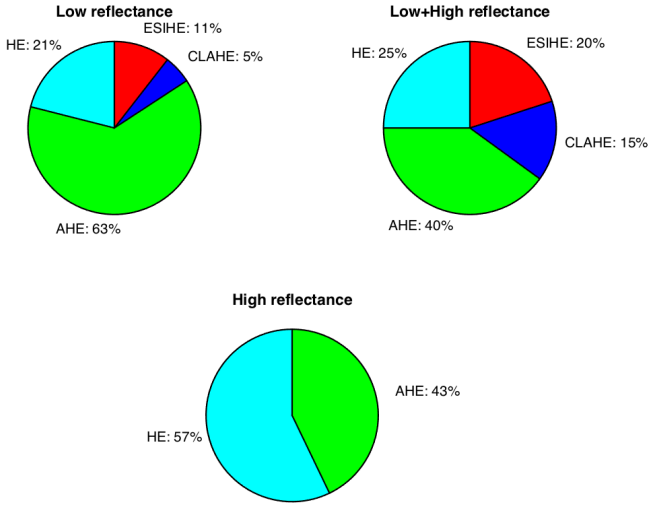

Figure 6.10: Image enhancement methods comparison with surface reflectance

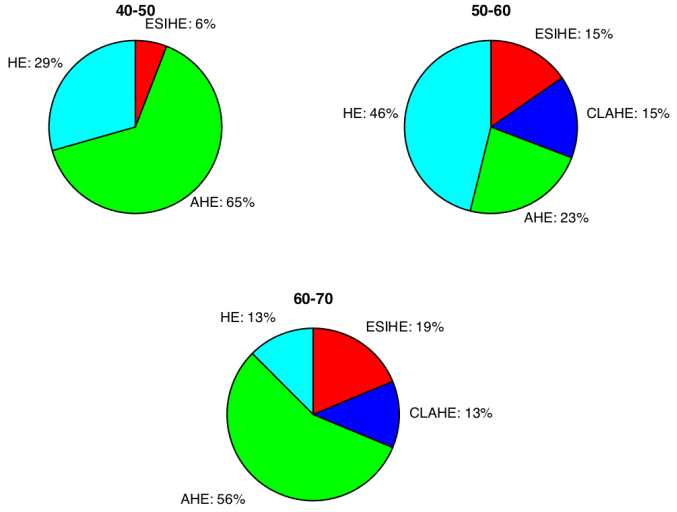

Figure 6.11: Image enhancement methods comparison with incidence angle

Figure: 6.11 shows the relation between the incidence angle and the enhancement methods. For low incidence angle the performance of HE and AHE are most suitable with a small percentage of ESIHE. For higher incidence angles, the percentage of CLAHE and ESIHE increases. CLAHE and ESIHE works well with high dynamic

range images, which occurs at low illumination due to high reflectance of smooth crater surface of new craters and sharp features like mountain peaks.

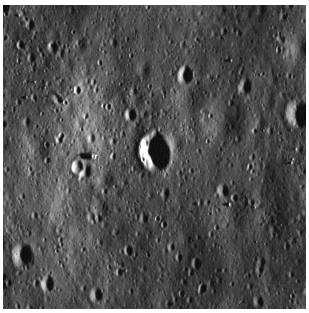

Figure 6.12: Image with incidence angle $i = 81.78^o$

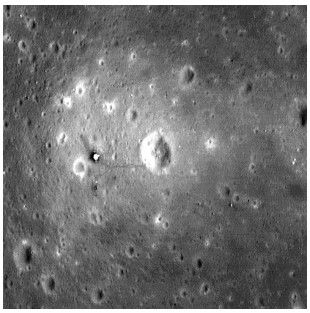

Figure 6.13: Image with incidence angle $i = 26.24^o$

Figures: 6.12 and 6.13 show the effect of both surface reflectance and incidence angle in one region. At high incidence angle ($i = 81.78^o$) the shadow appearance is strong and can be easily differentiated from the surface as shown in figure: 6.12. The shadows at high incidence angle can be segmented using a basic thresholding method, based on a threshold value (for example a pixel value less than 10 can be classified as shadow). Whereas, at low incidence angle ($i = 26.24^o$) the surface reflectance becomes prominent as evident in figure: 6.13. The cast shadow grey level from craters at the centre of the image appear similar to the grey value of the low reflectance surface at the border of the image, which can lead to false classification of the surface as shadow, even after enhancement. Hence, a high incidence angle is highly recommended for accurate shadow segmentation.

Objective classifier

As discussed earlier, only 46 images result in a unique enhancement methods. Out of these 46 images, 14 were selected to train the classifier as a training data set. The images in the training data set were selected from each of the enhancement methods. A maximum of 25% and minimum of 2 images were selected from each of the enhancement methods.

To establish a relationship between the classification parameters and the enhancement techniques, two methods were used. The first method was based on the confidence of the parameters. The confidence was based on the standard deviation, i.e. the lower the standard deviation the higher the confidence. Hence the weight was computed as the inverse of the standard deviation. The combination of the weighted values of the parameters was then used to classify the image. As shown in figure: 6.14, the performance of this classifier was not as desired and only 28.26% of the images were enhanced with the correct enhancement method.

On analysis it was observed that the parameter range for HE and AHE are very close and hence the classifier selects the enhancement methods (between HE and AHE) interchangeably. Further it was also observed that the performance of HE and AHE in terms of MSC percentage does not vary much (mentioned in appendix: F). Hence

the classification logic of HE and AHE were combined and treated as one method. As shown in figure: 6.14.c the combination of HE and AHE increases the correct enhancement method selection percentage to 55.56. Whereas at individual correct selection percentage for HE is 23.08 and for AHE is 17.39. Another interesting result is the correct selection percentage for CLAHE. As shown in figure: 6.14.c CLAHE has a correct selection percentage of 100 which shows that the classifier works perfectly in case of CLAHE. This is mainly because the weighted combine values of the images for which CLAHE is the best method are very unique. In case of ESIHE, the correct percentage is 33.33.

Another approach used to build the classifier logic was to use multi linear regression explained in appendix: E. Each of the enhancement methods were assigned a numerical value and used as dependent variable. The selected parameter values were considered as independent variable. The coefficients computed from the multi linear regression, were used to classify the test data. The output of the regression during the test, was bounded for a minimum and a maximum output value, based on the range of the numerical values assigned to the enhancement methods. As shown in figure: 6.14 the performance of the classifier is better than the weighted classifier with correct selection percentage of 50%. But it is still less than the desired value of 90%.

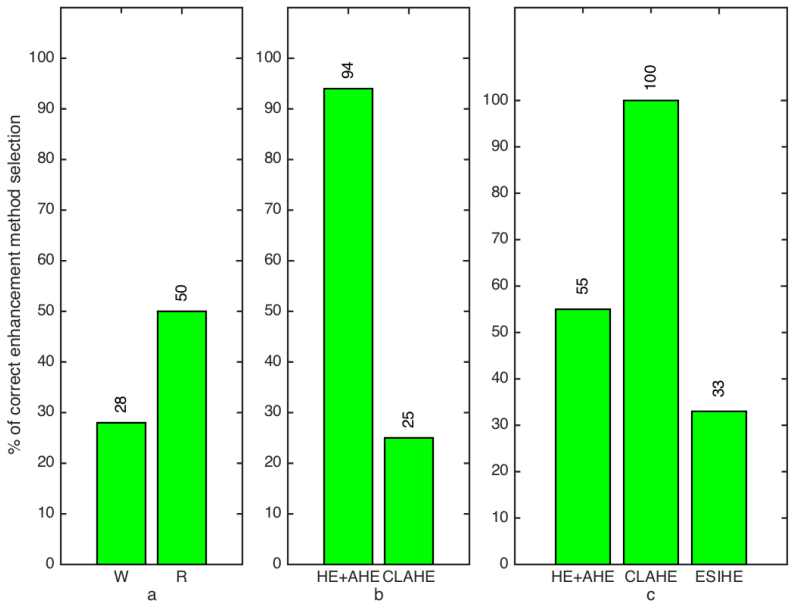

Figure 6.14: a. Performance of weighted (W) and regression based classifier (R), b. Performance of classifier for individual methods using regression, c. Performance of classifier for individual methods using weight

Figure: 6.14.b shows the correct selection percentage for the combination of HE and AHE to be 94.44. Whereas, the individual percentage for HE is 69.23 and of AHE is 56.52. The performance for CLAHE and ESIHE is not as desired. The correct

selection percentage of CLAHE is 25 and correct selection percentage for ESIHE is 0. The performance gap for CLAHE and ESIHE is attributed to the availability of less amount of training data for CLAHE and ESIHE.

6.3 Discussion

Experimental results show that image enhancement is necessary for a better performance of the BSM, as the number of MSC from the shadow segmented enhanced images is higher compared to the number of MSC obtained from the original NAC images. In terms of individual performance, HE and AHE provide the highest percentage of MSC compared to CLAHE and ESIHE. The performance of AHE is good compared to other methods in terms of percentage of MSC points. The disadvantage of using AHE and HE is the number of USC points. The percentage of USC is very high in case of HE and AHE and the effect of high USC points on BSM needs to be checked.

The comparison of the enhancement methods with respect to the incidence angle shows that HE and AHE are dominating compared to CLAHE and ESIHE. But the performance of CLAHE and ESIHE increases with higher incidence angle. The analysis of the performance of enhancement algorithms with respect to the surface reflectance shows that the performance of AHE and HE are good for high or low reflectance regions. Whereas for regions combined with high and low reflectance surface the percentage performance of CLAHE and ESIHE increases. This supports the idea of selecting CLAHE and ESIHE as the suitable candidate for image enhancement of high dynamic range images (images with bright and dark region). It can also be concluded from these results that different enhancement algorithms are required for different images and hence an automated classification pipeline is required.

As discussed in chapter: 5 the major issue faced during the experiment was the spatial shift in the rendered images. The images rendered using the DTM models had spatial shift in both latitude and longitude compared to the corresponding NAC images. Due to the manual correction process required to correct the shift, the database available for testing was largely reduced.

Two methods were used to create the classification logic. In method one the parameter values were assigned a weight, based on the standard deviation, which was calculated from the tests with a training data set. A classification logic was developed using the combined weighted parameter values. Using this classification logic 28.26% of the images were enhanced with the correct method. The second method to design the classifier was to use the multi linear regression method, where each of the methods were assigned a numeric value and used as dependent variable. The parameter values were used as independent variable, and the obtained coefficients were used on the test data set. For 50% of the images, the selected enhancement method were correct when the classifier based on the multi linear regression was used. Both methods are below the desired 90% desired classifier performance.

On analysis it was observed that the parameter values of images for which HE and

AHE were best methods are similar and hence the classifier selects HE and AHE interchangeably. Another reason for the lag in the performance of the classifier was identified to be the lack of data. For the training of enhancement methods CLAHE and ESIHE only 2 images were available, which is not enough to decide the confidence or fit the model using multi-linear regression.

7 Summary and conclusion

This chapter starts with a summary of the thesis and how well the objectives were fulfilled. The next section gives an overview of the future improvements, by proposing possible solutions for the issues faced during the thesis, and the last section gives the conclusion.

7.1 Thesis summary

The BSM proposed by Kaufmann et al. [18] works on the principle of using shadows on the lunar surface for navigation. The shadows are identified as features and the pose of the landing spacecraft is estimated by comparing these features between a reference image and a real image. To test the concept Kaufmann has used rendered image for both, reference and descent image. As a next step it was necessary to test the BSM system with real lunar images. A preliminary analysis of real lunar images suggested that image enhancement is necessary to increase the number of segmented shadows.

Based on the preliminary analysis, two objectives were identified. The first objective was to look for an enhancement method, which is applicable on all the images. In case, one such algorithm is not available, the second objective was to set up an automatic pipeline for choosing the best enhancement method. The purpose of the pipeline is to classify an image based on visual information and parametric values, and enhance the image with the applicable enhancement algorithm.

For this purpose, data from the LRO mission was selected due to high resolution 2D NAC images and large amount of DTMs available for reference image rendering. As the performance of one enhancement method might not be suitable for all the images, as a first step NAC images were classified based on surface reflectance, topography and surface feature. The major factor affecting the enhancement method was considered to be the surface reflectance, as in the low reflectance region the surface can be misclassified as shadow, due to similar grey level values registered by the camera sensor. Various terrain and surface features such as craters mountains, rilles responsible for shadow generation on moon were also identified.

An image enhancement pipeline was implemented to classify and enhance the images automatically. The first stage of classification was to visually classify the images based on the scene information in the images, this is assumed to be prior mission knowledge. In the next stage the images were classified based on incidence angle[1] as the variation in illumination level affects the dynamic range of the images. Hence, the applied enhancement method might be different. Further the images were classified objectively, based on classification parameter values. The performance of the enhancement algorithms was tested by comparing the shadows segmented

[1] for a mission the incidence angle is known as the time of landing on the lunar surface is decided during the mission planning

from the enhanced NAC image with the shadows segmented from the rendered image. The selected enhancement algorithms were Histogram Equalisation (HE), Adaptive Histogram Equalisation (AHE), Contrast Limited Adaptive Histogram Equalisation (CLAHE), Exposure based Sub-Image Histogram Equalisation (ESIHE) and Homomorphic Filtering (HF).

The results show that, the enhancement of the real images is necessary. The number of the matched shadows between the rendered and the real images increases due to the applied enhancement. The most suitable image enhancement algorithms were the AHE and the HE, followed by the ESIHE and the CLAHE. The performance of the classifier was not as desired, but using multi-linear regression gives promising result for a combination of HE and AHE enhancement methods.

7.2 Future work and conclusion

As concluded in the previous section, it is required to enhance the images for correct shadow detection. HE and AHE were proposed to be the best candidate for image enhancement based on the available data, but they also provide a lot of USC points. The degradation in performance of BSM, due to the presence of the USC points in the images needs to be analysed. Although Kaufmann et al. [18] have given a low negative weight to USCs, a large number of USC points (as evident in HE and ALHE) might have an impact on the performance of BSM. The image rendering process does not include the reflectance of the lunar surface, this creates more shadows in the rendered image, compared to the NAC image. This happens because at low incidence angle the strength of the shadow for example, cast by a crater is reduced due to the lower surface reflectance of the Lunar surface. And since there is no surface reflectance in the current rendering process, the shadow cast by the same crater is much stronger in the virtual image. Hence, the reflectance factor should be included in the rendered image rendering process.

The major problem encountered during the thesis was with data to test the enhancement pipeline. Initially, it was decided to use 500 DTMs to test the pipeline, but due to the inaccurate ground lock of the DTMs and due to the time spent to fix the problem manually, the total number of DTMs to be used was reduced to 20. For the implementation of the proposed radiometric enhancement pipeline into a real mission, the performance should be further tested with a large data set.

One of the reason of the failure of the classifier, apart from the variation in different parameter values, is considered to be the small amount of data in the training data set. Weights allocated using a large data set might be more robust. The same is true for the regression method, as regression methods fit the model better with larger data set, with a larger training data set, the performance of the classifier might improve. As discussed in previous chapter the selection of the enhancement algorithms also depends on the incidence angle, hence it should also be included in the classifier.

BSM system estimates the pose of the spacecraft, by comparing the segmented shadows from the reference and the real image. The shadow segmentation in turn

depends on the contrast level of the image. The proposed image enhancement pipeline augments the shadow segmentation process by enhancing the contrast level of the image, which is vital for the performance of the BSM system.

References

[1] M. Bhat and M.S. Tarun Patil. "Adaptive clip limit for contrast limited adaptive histogram equalization (CLAHE) of medical images using least mean square algorithm". In: *Advanced Communication Control and Computing Technologies (ICACCCT), 2014 International Conference on*. 2014, pp. 1259–1263. DOI: 10.1109/ICACCCT.2014.7019300.

[2] Ernest Bowman-Cisneros. *LROC EDR/CDR Data Product Software Interface Specification*. Version 1.18. Arizona State University. June 2010.

[3] Ernest Bowman-Cisneros and Eric Eliason. *LROC RDR Data Products Software Interface Specification*. Version 1.4. Arizona State University. Mar. 2011.

[4] K. N. Burns et al. "DIGITAL ELEVATION MODELS AND DERIVED PRODUCTS FROM LROC NAC STEREO OBSERVATIONS". In: *ISPRS - International Archives of the Photogrammetry, Remote Sensing and Spatial Information Sciences* XXXIX-B4 (2012), pp. 483–488. DOI: 10.5194/isprsarchives-XXXIX-B4-483-2012. URL: http://www.int-arch-photogramm-remote-sens-spatial-inf-sci.net/XXXIX-B4/483/2012/.

[5] David A Clausi. "An analysis of co-occurrence texture statistics as a function of grey level quantization". In: *Canadian Journal of remote sensing* 28.1 (2002), pp. 45–62.

[6] ESA. *Spece Engineering and Technology*. 2015. URL: http://www.esa.int/Our_Activities/Space_Engineering_Technology/Pinpoint_vision-based_landings_on_Moon_Mars_and_asteroids (visited on 02/09/2015).

[7] Antonio Fernández-Caballero et al. "Optical flow or image subtraction in human detection from infrared camera on mobile robot". In: *Robotics and Autonomous Systems* 58.12 (2010). Intelligent Robotics and Neuroscience, pp. 1273 –1281. ISSN: 0921-8890. DOI: http://dx.doi.org/10.1016/j.robot.2010.06.002. URL: http://www.sciencedirect.com/science/article/pii/S0921889010001168.

[8] Bruce L. Gary and David Healy. *Image Subtraction Procedure For Observing Faint Asteroids*. 2015. URL: http://brucegary.net/ist/MPB_46053.htm.

[9] Rafael C. Gonzalez and Richard E. Woods. *Digital Image Processing*. 3rd ed. Prentice Hall, 2008.

[10] R.M. Haralick and K. Shanmugam. "Computer Classification of Reservoir Sandstones". In: *Geoscience Electronics, IEEE Transactions on* 11.4 (1973), pp. 171–177. ISSN: 0018-9413. DOI: 10.1109/TGE.1973.294312.

[11] Dong-Chen He and Li Wang. "Texture Unit, Texture Spectrum, And Texture Analysis". In: *Geoscience and Remote Sensing, IEEE Transactions on* 28.4 (1990), pp. 509–512. ISSN: 0196-2892. DOI: 10.1109/TGRS.1990.572934.

[12] T. Jintasuttisak and S. Intajag. "Color retinal image enhancement by Rayleigh contrast-limited adaptive histogram equalization". In: *Control, Automation and Systems (ICCAS), 2014 14th International Conference on*. 2014, pp. 692–697. DOI: 10.1109/ICCAS.2014.6987868.

[13] A.E. Johnson and J.F. Montgomery. "Overview of Terrain Relative Navigation Approaches for Precise Lunar Landing". In: *Aerospace Conference, 2008 IEEE*. Mar. 2008, pp. 1–10. DOI: 10.1109/AERO.2008.4526302.

[14] Eric M. Jones and Ken Glover. *Lunar Surface Journal*. 2015. URL: https://www.hq.nasa.gov/alsj/.

[15] M.K. Kaiser, N.R. Gans, and W.E. Dixon. "Vision-Based Estimation for Guidance, Navigation, and Control of an Aerial Vehicle". In: *Aerospace and Electronic Systems, IEEE Transactions on* 46.3 (July 2010), pp. 1064–1077. ISSN: 0018-9251. DOI: 10.1109/TAES.2010.5545174.

[16] J.N. Kapur, P.K. Sahoo, and A.K.C. Wong. "A new method for gray-level picture thresholding using the entropy of the histogram". In: *Computer Vision, Graphics, and Image Processing* 29.3 (1985), pp. 273 –285. ISSN: 0734-189X. DOI: http://dx.doi.org/10.1016/0734-189X(85)90125-2. URL: http://www.sciencedirect.com/science/article/pii/0734189X85901252.

[17] Hannah Kaufmann. "Shadow-based matching for robust absolute localization during lunar landings". MA thesis. Technische Universität Berlin, 2014.

[18] Hannah Kaufmann et al. "Shadow-based matching for precise and robust absolute self-localization during lunar landings". In: *Aerospace Conference, 2015 IEEE*. 2015, pp. 1–13. DOI: 10.1109/AERO.2015.7119045.

[19] David J. Ketcham, Roger W. Lowe, and J. William Weber. *Image enhancement techniques for cockpit displays*. Tech. rep. Hughes Aircraft Company.

[20] Jia Longhao, Zhou Zhongfa, and Li Bo. "Study of SAR Image Texture Feature Extraction Based on GLCM in Guizhou Karst Mountainous Region". In: *Remote Sensing, Environment and Transportation Engineering (RSETE), 2012 2nd International Conference on*. 2012, pp. 1–4. DOI: 10.1109/RSETE.2012.6260741.

[21] T. Miso, T. Hashimoto, and K. Ninomiya. "Optical guidance for autonomous landing of spacecraft". In: *Aerospace and Electronic Systems, IEEE Transactions on* 35.2 (1999), pp. 459–473. ISSN: 0018-9251. DOI: 10.1109/7.766929.

[22] D. Mitrea, S. Nedevschi, and R. Badea. "The role of the superior order GLCM in improving the automatic diagnosis of the hepatocellular carcinoma based on ultrasound images". In: *Telecommunications and Signal Processing (TSP), 2011 34th International Conference on*. 2011, pp. 602–606. DOI: 10.1109/TSP.2011.6043658.

[23] Thomas B. Moeslund. *Introduction to Video and Image Processing*. 1st ed. Springer London, 2012.

[24] Douglas C. Montgomery, Elizabeth A. Peck, and G. Geoffrey Vining. *Introduction to Linear Regression Analysis*. 5th ed. Wiley, 2012.

[25] NASA. *APOLLO OVER THE MOON: A VIEW FROM ORBIT*. 2015. URL: http://history.nasa.gov/SP-362/ch6.3.htm (visited on 08/04/2015).

[26] NASA. *Beyond Earth*. 2015. URL: http://www.nasa.gov/exploration/home/why_moon_objectives.html (visited on 03/01/2015).

[27] NASA/Goddard. *Lunar Reconnaissance Orbiter*. 2015. URL: http://lro.gsfc.nasa.gov/index.html (visited on 06/11/2015).

[28] NASA/JPL-Caltech/ESA. *Landing Accuracy on Mars*. 2015. URL: http://mars.jpl.nasa.gov/msl/multimedia/images/?ImageID=4398 (visited on 02/05/2015).

[29] NASA/NAIF. *SPICE Data*. 2015. URL: http://naif.jpl.nasa.gov/naif/data.html (visited on 06/26/2015).

[30] NOAA. *XYZ Conversion*. 2015. URL: http://www.ngs.noaa.gov/TOOLS/XYZ/xyz.html (visited on 06/26/2015).

[31] NVIDIA. *Developer Zone*. 2015. URL: http://http.developer.nvidia.com/GPUGems3/gpugems3_ch08.html (visited on 07/12/2015).

[32] Stephen M. Pizer et al. "Adaptive Histogram Equalization and Its Variations". In: *Computer Vision, Graphics, and Image Processing 39*. Oct. 1986, pp. 355–368.

[33] William K. Pratt. *Digital Image Processing*. 2nd ed. John Wiley & Sons, INC., 1991.

[34] Motong Qiao and Michael K. Ng. "Tone mapping for high-dynamic-range images using localized gamma correction". In: *Journal of Electronic Imaging* 24.1 (2015), p. 013010. DOI: 10.1117/1.JEI.24.1.013010. URL: http://dx.doi.org/10.1117/1.JEI.24.1.013010.

[35] M.S. Robinson et al. "Lunar Reconnaissance Orbiter Camera (LROC) Instrument Overview". English. In: *Space Science Reviews* 150.1-4 (2010), pp. 81–124. ISSN: 0038-6308. DOI: 10.1007/s11214-010-9634-2. URL: http://dx.doi.org/10.1007/s11214-010-9634-2.

[36] Julio Sanchez and Maria P. Canton. *Space Image Processing*. 1st ed. CRC Press, 1998.

[37] Julio Sanchez and Maria P. Canton. *Space Image Processing with Cdrom*. 1st. Boca Raton, FL, USA: CRC Press, Inc., 1998. ISBN: 0849331137.

[38] J. Scott and M. Pusateri. "Towards real-time hardware gamma correction for dynamic contrast enhancement". In: *Applied Imagery Pattern Recognition Workshop (AIPRW), 2009 IEEE*. Oct. 2009, pp. 1–5. DOI: 10.1109/AIPR.2009.5466305.

[39] Kuldeep Singh and Rajiv Kapoor. "Image enhancement using Exposure based Sub Image Histogram Equalization". In: *Pattern Recognition Letters* 36.0 (2014), pp. 10 –14. ISSN: 0167-8655. DOI: http://dx.doi.org/10.1016/j.patrec.2013.08.024. URL: http://www.sciencedirect.com/science/article/pii/S0167865513003280.

[40] Huihui Song, Bo Huang, and Kaihua Zhang. "Shadow Detection and Reconstruction in High-Resolution Satellite Images via Morphological Filtering and Example-Based Learning". In: *Geoscience and Remote Sensing, IEEE Transactions on* 52.5 (2014), pp. 2545–2554. ISSN: 0196-2892. DOI: 10.1109/TGRS.2013.2262722.

[41] United States Geological Survey. *Glossary*. 2015. URL: http://isis.astrogeology.usgs.gov/documents/Glossary/Glossary.html#IncidenceAngle (visited on 03/05/2015).

[42] Gregory Y. Tang. "A Discrete Version of Green's Theorem". In: *Pattern Analysis and Machine Intelligence, IEEE Transactions on* PAMI-4.3 (1982), pp. 242–249. ISSN: 0162-8828. DOI: 10.1109/TPAMI.1982.4767241.

[43] M. Umaselvi, S.S. Kumar, and M. Athithya. "Color based Urban and Agricultural Land classification by GLCM Texture Features". In: *Sustainable Energy and Intelligent Systems (SEISCON 2012), IET Chennai 3rd International on*. 2012, pp. 1–4. DOI: 10.1049/cp.2012.2213.

[44] Arizona State University. *LROC*. 2015. URL: http://wms.lroc.asu.edu/lroc/search (visited on 02/09/2015).

[45] Arizona State University. *LROC*. 2015. URL: http://www.lroc.asu.edu/.

[46] Arizona State University. *LROC*. 2015. URL: http://www.lroc.asu.edu/posts/5 (visited on 07/12/2015).

[47] Arizona State University. *LROC*. 2015. URL: http://wms.lroc.asu.edu/lroc/rdr_product_select#_ui-id-1 (visited on 02/09/2015).

[48] Ting Yun and Huazhong Shu. "Ultrasound image segmentation by spectral clustering algorithm based on the curvelet and GLCM features". In: *Electrical and Control Engineering (ICECE), 2011 International Conference on*. 2011, pp. 920–923. DOI: 10.1109/ICECENG.2011.6057730.

[49] Wang Zhiming and Tao Jianhua. "A Fast Implementation of Adaptive Histogram Equalization". In: *Signal Processing, 2006 8th International Conference on*. Vol. 2. 2006, pp. –. DOI: 10.1109/ICOSP.2006.345602.

[50] Karel Zuiderveld. "Graphics Gems IV". In: ed. by Paul S. Heckbert. San Diego, CA, USA: Academic Press Professional, Inc., 1994. Chap. Contrast Limited Adaptive Histogram Equalization, pp. 474–485. ISBN: 0-12-336155-9. URL: http://dl.acm.org/citation.cfm?id=180895.180940.

A Selected DTM and NAC pair

Table: A1 shows the DTM-NAC pair selected to validate the radiometric enhancement pipeline. In the table i is the incidence angle.

DTM	NAC	i
NAC_DTM_MAUROLYCS	M1162384686RE	44.75
NAC_DTM_PITISCUS	M1149280834RE	53.42
NAC_DTM_WHALE	M1114490755RE	45.6
NAC_DTM_LARMORQ4	M1097686764RE	60.1
NAC_DTM_BUFFON	M1117380495RE	47.22
NAC_DTM_CAUCHY	M1108039362RE	63.38
NAC_DTM_CHAPPELLT	M1117723384RE	52.48
NAC_DTM_LAPLACEA	M1103723246RE	47.83
NAC_DTM_HARDINGH	M173327696RE	45.89
NAC_DTM_FOWLERSCRP	M143221393RE	53.5
NAC_DTM_FRSHCRATER13	M185396720RE	59.02
NAC_DTM_HANSTEENAL3	M181494651RE	62.91
NAC_DTM_MANILUS	M1121188383RE	43.99
NAC_DTM_MOSCOVNSE1	M158999646RE	45.14
NAC_DTM_POSIDONIUS	M1098658474RE	53.15
NAC_DTM_PRINZVENT	M1129759205RE	47.67
NAC_DTM_ROSSELAND2	M1135724889RE	44.84
NAC_DTM_VSCHROTERI	M1114497847RE	43.54
NAC_DTM_GRUITHUIS10	M160221419RE	58.61
NAC_DTM_BHABHAPLAIN	M112653051RE	63.12

Table A1: Selected DTM-NAC pair

B Adjustment to fix the spatial shift

Table:B1 gives the pitch (θ), roll (ψ) and yaw (ϕ) values used and the manual offset (ΔR and ΔC) used to match the spatial shift. The table also provides the spatial resolution (Scale) of the rendered virtual image.

DTM	NAC	θ	ΔR	ΔC	Scale
NAC_DTM_MAUROLYCS	M1162384686RE	0	85	-10	8
NAC_DTM_PITISCUS	M1149280834RE	0	37	-19	8
NAC_DTM_WHALE	M1114490755RE	0	82	-12	20
NAC_DTM_LARMORQ4	M1097686764RE	0	29	3	20
NAC_DTM_BUFFON	M1117380495RE	-0.15	-4	-14	8
NAC_DTM_CAUCHY	M1108039362RE	-0.3	0	0	20
NAC_DTM_CHAPPELLT	M1117723384RE	-0.25	0	0	20
NAC_DTM_LAPLACEA	M1103723246RE	0	0	0	20
NAC_DTM_HARDINGH	M173327696RE	0	0	0	8
NAC_DTM_FOWLERSCRP	M143221393RE	-0.15	0	0	8
NAC_DTM_FRSHCRATER13	M185396720RE	-0.35	0	0	8
NAC_DTM_HANSTEENAL3	M181494651RE	-0.45	0	0	20
NAC_DTM_MANILUS	M1121188383RE	0.7	0	0	20
NAC_DTM_MOSCOVNSE1	M158999646RE	0.2	0	0	8
NAC_DTM_POSIDONIUS	M1098658474RE	-0.49	0	0	20
NAC_DTM_PRINZVENT	M1129759205RE	-0.52	0	0	20
NAC_DTM_ROSSELAND2	M1135724889RE	-0.05	0	0	12
NAC_DTM_VSCHROTERI	M1114497847RE	-0.4	0	0	20
NAC_DTM_GRUITHUIS10	M160221419RE	0	0	0	0
NAC_DTM_BHABHAPLAIN	M112653051RE	0	0	0	8

Table B1: Calibration information of DTM-NAC pair

C Rendering resolution of DTM and NAC images

Table:C1 gives the rendering resolution of all the DTM and NAC images using the formula explained in chapter: 5.

DTM	NAC	Row	Column
NAC_DTM_MAUROLYCS	M1162384686RE	4361	423
NAC_DTM_PITISCUS	M1149280834RE	3244	315
NAC_DTM_WHALE	M1114490755RE	2845	276
NAC_DTM_LARMORQ4	M1097686764RE	3885	377
NAC_DTM_BUFFON	M1117380495RE	4218	409
NAC_DTM_CAUCHY	M1108039362RE	3120	303
NAC_DTM_CHAPPELLT	M1117723384RE	4154	403
NAC_DTM_LAPLACEA	M1103723246RE	4308	418
NAC_DTM_HARDINGH	M173327696RE	3361	326
NAC_DTM_FOWLERSCRP	M143221393RE	4342	421
NAC_DTM_FRSHCRATER13	M185396720RE	3412	331
NAC_DTM_HANSTEENAL3	M181494651RE	2552	248
NAC_DTM_MANILUS	M1121188383RE	2953	287
NAC_DTM_MOSCOVNSE1	M158999646RE	4252	413
NAC_DTM_POSIDONIUS	M1098658474RE	3792	368
NAC_DTM_PRINZVENT	M1129759205RE	3475	337
NAC_DTM_ROSSELAND2	M1135724889RE	3109	302
NAC_DTM_VSCHROTERI	M1114497847RE	3435	334
NAC_DTM_GRUITHUIS10	M160221419RE	3235	313
NAC_DTM_BHABHAPLAIN	M112653051RE	4075	395

Table C1: Selectted resolution of DTM-NAC pair

D Surface features covered by NAC images

Table:D1 lists the surface reflectance, terrain and surface features contained by selected NAC images. The acronyms used in the table are explained below:

B: Boulder
CC: Chained Crater
F: Fracture
FS: Flat Surface
G: Graben
H(T): High reflectance region (Terra)
L(M): Low reflectance region (Marre)
R: Rilles
WR: Wrinkled Ridges

DTM	NAC	Surface reflectance	Terrain	Surface feature
NAC_DTM_MAUROLYCS	M1162384686RE	L(M)	FS	CC, OC, NC, R
NAC_DTM_PITISCUS	M1149280834RE	H(T)	FS	OC, NC, R
NAC_DTM_WHALE	M1114490755RE	L(M)	FS, WR	OC, NC
NAC_DTM_LARMORQ4	M1097686764RE	L(M)	FS, B	OC
NAC_DTM_BUFFON	M1117380495RE	L(M)	FS, G	OC, NC
NAC_DTM_CAUCHY	M1108039362RE	H(T)	FS, G	OC, NC
NAC_DTM_CHAPPELLT	M1117723384RE	L(M)	FS, WR	OC
NAC_DTM_LAPLACEA	M1103723246RE	H(T)	FS	OC
NAC_DTM_HARDINGH	M173327696RE	H(T)	FS	OC
NAC_DTM_FOWLERSCRP	M143221393RE	H(T)	FS, WR	OC
NAC_DTM_FRSHCRATER13	M185396720RE	H(T)	FS, B	OC
NAC_DTM_HANSTEENAL3	M181494651RE	L(M)	FS, WR	OC
NAC_DTM_MANILUS	M1121188383RE	L(M)	FS, WR	OC
NAC_DTM_MOSCOVNSE1	M158999646RE	L(M)	FS	OC
NAC_DTM_POSIDONIUS	M1098658474RE	H(T)	FS, R	OC
NAC_DTM_PRINZVENT	M1129759205RE	L(M)	FS, G, R	OC
NAC_DTM_ROSSELAND2	M1135724889RE	L(M)	FS	OC
NAC_DTM_VSCHROTERI	M1114497847RE	L(M)	FS, F	OC
NAC_DTM_GRUITHUIS10	M160221419RE	H(T)	FS, WR	OC
NAC_DTM_BHABHAPLAIN	M112653051RE	H(T)	FS	OC, NC

Table D1: Surface and terrain information of DTM-NAC pair

E Multi linear regression

The multi linear regression mean function [24] [page: 67] used for to fit the model between the parameters and the enhancement algorithms is shown in equation: E1

$$E(Y|X) = \beta_1 X_1 + \beta_2 X_2 + \beta_3 X_3 + \beta_4 X_4 \tag{E1}$$

where, Y is the response vector of the dependent values. In this case the numerical values assigned to each of the enhancement methods, shown in table: E1

Method	Numerical values
HE	1
AHE	2
CLAHE	3
ESIHE	4

Table E1: Numerical values assigned to each method

X is the design matrix, and β is the slope for individual parameters. Equation: E1 can be represented as $Y = X\beta$. The objective is to find the β values using least mean square error approach. For this purpose the equation: E2 should be minimised.

$$\sum (Y - \beta X)^2 \tag{E2}$$

After differentiating the equation: E2 and rearranging the β value can be calculated by equation: E3

$$\beta = (X'X)^{-1}X'Y \tag{E3}$$

F Matched shadows for each enhancement method, for the selected images

Image	HE	AHE	CLAHE	ESIHE	HF	OI
M1162384686RE_0	100	100	100	100	100	100
M1162384686RE_1	100	100	100	100	100	100
M1162384686RE_2	87.500	87.500	87.500	87.500	87.500	87.500
M1162384686RE_4	66.667	66.667	66.667	66.667	66.667	66.667
M1149280834RE_1	100	100	100	100	0	0
M1114490755RE_0	41.667	50	33.333	0	0	0
M1114490755RE_1	85.714	100	71.428	57.143	28.571	28.571
M1114490755RE_2	62.500	62.500	37.500	37.500	12.500	0
M1114490755RE_3	81.818	36.364	45.454	63.636	0	0
M1114490755RE_4	44.444	44.444	33.333	22.222	0	0
M1097686764RE_0	8.3333	11.111	2.778	13.889	2.778	2.778
M1097686764RE_1	17.78	28.889	11.111	15.555	2.2222	2.2222
M1097686764RE_2	20.833	27.083	22.917	22.917	2.0833	2.0833
M1097686764RE_3	8.064	17.742	9.677	9.677	0	0
M1097686764RE_4	17.857	21.428	10.714	19.643	5.3571	5.3571
M1108039362RE_0	87.234	87.234	4.255	14.894	0	0
M1108039362RE_1	70.588	64.706	8.823	38.235	2.941	2.941
M1108039362RE_2	66.667	84.444	6.667	6.667	2.222	0
M1108039362RE_3	78.571	83.928	8.928	76.785	0	0
M1108039362RE_4	86.956	84.782	15.217	69.565	0	0
M1117723384RE_0	33.333	30.158	11.111	23.809	1.587	1.587
M1117723384RE_1	50	50	0	50	0	0
M1117723384RE_2	54.545	36.364	13.636	45.454	0	0
M1117723384RE_3	36.170	51.064	2.128	21.28	2.128	2.128
M1117723384RE_4	44.444	40.741	25.926	40.741	7.407	7.407
M1103723246RE_0	22.727	27.273	0	18.182	0	0
M1103723246RE_1	37.500	37.500	0	56.250	6.2500	0
M1103723246RE_2	40	53.333	0	20	0	0
M1103723246RE_3	71.428	74.285	11.428	60	0	0
M1103723246RE_4	75	75	0	33.333	0	0
M173327696RE_2	100	100	100	100	100	100
M173327696RE_4	100	100	100	100	66.667	66.667
M185396720RE_2	78.8	60.606	18.182	69.697	0	0
M185396720RE_3	59.091	68.182	27.273	77.273	0	0
M185396720RE_4	80	60	60	80	0	0
M181494651RE_0	69.231	69.231	10.256	70.513	5.128	5.128
M181494651RE_1	58.889	66.667	2.2222	58.889	1.1111	1.1111
M181494651RE_2	30.303	30.303	12.121	24.242	3.0303	0
M181494651RE_3	28.571	57.143	0	9.524	0	0
M181494651RE_4	23.529	20.588	29.412	5.882	2.941	2.941
M1121188383RE_0	42.857	42.857	28.571	42.857	0	0
M1121188383RE_1	71.428	85.714	57.143	71.428	28.571	14.285
M1121188383RE_2	100	100	100	100	16.667	16.667
M1121188383RE_3	100	50	50	50	0	50
M1121188383RE_4	62.500	37.500	25	37.500	25	25
M158999646RE_3	100	100	100	100	100	100
M158999646RE_4	100	100	100	100	100	100
M1098658474RE_0	62.500	75	12.500	62.500	0	0
M1098658474RE_1	23.809	42.857	19.048	47.619	0	0
M1098658474RE_2	47.059	35.294	47.059	35.294	0	0
M1098658474RE_3	41.379	51.724	48.276	44.827	0	0
M1098658474RE_4	47.059	44.118	20.588	20.588	0	0
M1129759205RE_0	87.500	87.500	87.500	87.500	75	62.500
M1129759205RE_1	94.118	94.118	94.118	94.118	47.059	47.059
M1129759205RE_2	88.461	96.154	84.615	88.461	34.615	69.231
M1129759205RE_3	82.353	82.353	64.706	76.470	52.941	52.941
M1129759205RE_4	41.667	16.667	25	16.667	16.667	16.667
M1135724889RE_0	50	100	50	50	0	0
M1135724889RE_4	65.517	72.414	41.379	72.414	0	0
M1114497847RE_0	63.636	81.818	0	54.545	0	0
M1114497847RE_1	50	64.285	0	57.143	0	0
M1114497847RE_2	37.500	37.500	0	37.500	0	0
M1114497847RE_3	50	0	0	0	0	0
M1114497847RE_4	62.500	75	0	62.500	0	0
M160221419RE_0	70	80	90	70	0	0
M160221419RE_1	100	85.714	85.714	57.143	0	0
M160221419RE_2	100	100	50	0	0	0
M160221419RE_3	20	20	60	0	0	0
M160221419RE_4	75	75	75	37.500	0	0
M112653051RE_0	50	25	75	50	0	0
M112653051RE_1	75	100	100	75	25	25
M112653051RE_2	62.500	75	75	75	12.500	12.500
M112653051RE_3	47.059	41.176	47.059	64.706	11.765	11.765
M112653051RE_4	75	100	50	75	25	25

Table F1: MSC % of each enhancement method for the selected 74 images